STUDY OF HYPERFINE STRUCTURES OF RUBIDIUM
BY DOPPLER-FREE SATURATED
ABSORPTION SPECTROSCOPY

ATHIP CHAYAKUL

MASTER OF SCIENCE
IN PHYSICS

THE GRADUATE SCHOOL
CHIANG MAI UNIVERSITY
MAY 2012

STUDY OF HYPERFINE STRUCTURES OF RUBIDIUM BY DOPPLER-FREE SATURATED ABSORPTION SPECTROSCOPY

ATHIP CHAYAKUL

A THESIS SUBMITTED TO THE GRADUATE SCHOOL IN
PARTIAL FULFILLMENT OF THE REQUIREMENTS
FOR THE DEGREE OF
MASTER OF SCIENCE
IN PHYSICS

THE GRADUATE SCHOOL
CHIANG MAI UNIVERSITY
MAY 2012

STUDY OF HYPERFINE STRUCTURES OF RUBIDIUM BY DOPPLER-FREE SATURATED ABSORPTION SPECTROSCOPY

ATHIP CHAYAKUL

THIS THESIS HAS BEEN APPROVED
TO BE A PARTIAL FULFILLMENT OF THE REQUIREMENTS
FOR THE DEGREE OF MASTER OF SCIENCE
IN PHYSICS

EXAMINING COMMITTEE

S. Duangthai .... CHAIRPERSON
Dr. Sangwahn Duangthai

Chuleeporn .... MEMBER
Assoc. Prof. Dr. Chuleeporn Wongtawatnugool

.... MEMBER
Asst. Prof. Dr. Duangmanee Wongratanaphisan

.... MEMBER
Dr. Waranont Anukool

THESIS ADVISORY COMMITTEE

.... ADVISOR
Dr. Waranont Anukool

.... CO-ADVISOR
Assoc. Prof. Dr. Chuleeporn Wongtawatnugool

23 May 2012

ACKNOWLEDGEMENT

In the course of my study, I have been very fortunate to receive assistances and supports from many people, all those who gave me the possibility to complete this thesis, to whom I would like to express my sincere gratitude.

First, I gratefully acknowledge my supervisor Dr. Waranont Anukool for his supervision, encouragement, suggestions and supports during the time of this research. He spent endless time sharing his experiences and advices beneficial for conducting any kind of researches in the future. He also motivated and inspired me every single time I talked to him. He made me felt in love with Quantum Mechanics especially.

I would like also to thank Assoc. Prof. Dr. Teparksorn Pengpan. He originally introduced me basic concepts of Quantum Mechanics when I was the third year undergraduate student. He made me bewitched in this subject as well.

During my study for the master degree of science in physics at Chiang Mai University (CMU), I appreciatively acknowledged Dr. Sangwahn Duangthai who introduced me in more details atomic and molecular spectroscopy. She gave me precious suggestions as well as encouragement since I knew her until now. I would like to acknowledge Asst. Prof. Dr. Duangmanee Wongratanaphisan for her kindness and taking care of me in the first year at CMU including her suggestions. I would like to thanks Assoc. Prof. Dr. Chuleeporn Wongtawatnugool for encouragement, suggestions and supports.

I would like to express special acknowledgement to Dr. Narupon Chattrapiban for his collaborations and invaluable supports (T^T). Without him this work would not be completed well. I learned a great deal of necessary skills and knowledge from him.

In addition to their friendship, I would like to thank my colleagues for their helps and contributions. I truely appreciated the warm atmosphere in the Quantum Atom Optics Laboratory (QAO) from P. Sompet, C. Kamrapis, N. Thaicharoen, P. Chaiwongkot, T. Poomaradee, R. Kaewuam, and C. Saisa-ard. Especially thanks to P. Sompet, N. Thaicharoen, and T. Poomaradee for their kind supports in electronic works. I wanted to thank them all for their supports and worthful suggestions.

I desire to express my gratefulness to Kamrapis family for all supports and consolation. I also want to thank A. Kanjai for his encouragement. My special thank also convey to funding agencies including DPST and ThEP. Furthermore, I would like to express my apology that I could not mention many people personally one by one.

Finally, I would like to dedicate this dissertation to my family especially my mother and father, whose love and care empower me to complete this work. It is my pleasure to express my gratitude from the bottom of my heart to them all.

Athip Chayakul

Thesis Title Study of Hyperfine Structures of Rubidium by Doppler-free Saturated Absorption Spectroscopy

Author Mr. Athip Chayakul

Degree Master of Science (Physics)

Thesis Advisory Committee

Dr. Waranont Anukool	Advisor
Assoc. Prof. Dr. Chuleeporn Wongtawatnugool	Co-advisor

ABSTRACT

As a key step toward laser cooling and trapping of neutral atoms, the Doppler-free saturated absorption spectroscopy was conducted to resolve the true nature of intrinsic hyperfine energy splitting in gaseous rubidium 85 and 87 from the atomic motional effect. The absorption spectra were obtained by linearly scanning the frequency of a home-built external cavity diode laser over the range of D_2 line. The Doppler broadening was suppressed due to a narrow velocity selection involving a pair of counter-propagating beams. Two optical schemes associating with pump and probe beams i.e., the small-angled cross beam and the antiparallel beam configurations were performed. The resolvability of absorption linewidth was found that both optical arrangements have no significant advantage over one another.

ชื่อเรื่องวิทยานิพนธ์ การศึกษาโครงสร้างไฮเปอร์ไฟน์ของรูบิเดียมโดยสเปกโตรสโคปีชนิดดูดกลืนอิ่มตัวแบบปราศจากดอปเปลอร์

ผู้เขียน นายอธิป ฉายากุล

ปริญญา วิทยาศาสตรมหาบัณฑิต (ฟิสิกส์)

คณะกรรมการที่ปรึกษาวิทยานิพนธ์

ดร.วรานนท์ อนุกูล	อาจารย์ที่ปรึกษาหลัก
รศ. ดร.ชุลีพร วงศ์ธวัชนุกูล	อาจารย์ที่ปรึกษาร่วม

บทคัดย่อ

สเปกโตรสโคปีชนิดดูดกลืนอิ่มตัวแบบปราศจากดอปเปลอร์เป็นกลวิธีในการแยกโครงสร้างละเอียดไฮเปอร์ที่แท้จริงของอะตอมรูบิเดียมไอโซโทป 85 และ 87 ในสถานะก๊าซออกจากอิทธิพลของการเคลื่อนที่ของอะตอม ซึ่งเป็นกุญแจสำคัญที่นำไปสู่การทำความเย็นและกักขังอะตอมที่เป็นกลางทางไฟฟ้าด้วยเลเซอร์ สเปกตรัมการดูดกลืนได้มาจากการเปลี่ยนความถี่อย่างเชิงเส้นของเลเซอร์แบบช่องภายนอกบนช่วงสเปกตรัมเส้น D_2 การกว้างออกชนิดดอปเปลอร์ของสเปกตรัมถูกกดข่มได้ด้วยการเลือกความเร็วในช่วงแคบที่เกิดจากคู่ของลำแสงที่สวนทางกัน งานวิจัยนี้ได้แสดงการทดลองในสองรูปแบบเกี่ยวเนื่องกับลำแสงปั๊มและลำแสงตรวจสอบ ซึ่งทั้งสองลำแสงเคลื่อนที่ในทิศสวนทางกันตัดกันเป็นมุมขนาดเล็กและเคลื่อนที่ซ้อนทับกัน จากการทดลองพบว่าการแยกของไลน์วิดธ์การดูดกลืนจากการทดลองในสองรูปแบบไม่แสดงให้เห็นว่าการทดลองแบบหนึ่งแบบใดดีกว่ากัน

TABLE OF CONTENTS

LIST OF TABLES

LIST OF FIGURES

ABBREVIATIONS AND SYMBOLS

AMO	Atomic, molecular, and optical physics
ECDL	External cavity diode laser
d	Groove spacing (pitch) of grating
θ_i	Incident angle
φ_m	Diffracted angle
λ	Wavelength of laser
$\boldsymbol{\mu}_\mathbf{L}$	Magnetic dipole moment of orbital angular momentum
g_L	Magnetogyric ratio of the orbital magnetic moment
μ_B	Bohr's magnetron
$\mathbf{L}$	Orbital angular momentum
$\hbar$	Reduced Planck's constant
$\boldsymbol{\mu}_\mathbf{S}$	Magnetic dipole moment of spin angular momentum
g_S	Magnetogyric ratio of the spin magnetic moment

$\mathbf{S}$	Spin angular momentum
$\boldsymbol{\mu}_\mathbf{J}$	Magnetic dipole moment of total angular momentum
g_J	Landè-factor
$\mathbf{J}$	Total orbital-spin angular momentum
$\mathbf{I}$	Nuclear spin angular momentum
$\boldsymbol{\mu}_\mathbf{I}$	Magnetic dipole moment of nuclear spin angular momentum
μ_N	Nuclear magnetron
m_p	Mass of proton
g_I	Magnetogyric ratio of the nuclear spin magnetic moment
e	Electronic charge
$E_{L,S}$	LS-coupling energy
$\mathbf{B}_\mathbf{L}$	Magnetic field related to the orbital motion of electron
a^*	Fine structure constant
Z	Nuclear charge
n	Principal quantum number
L	Orbital angular momentum quantum number
$\mathbf{B}_\mathbf{J}$	Magnetic field related to orbital motion and spin of the electrons

$\mathbf{F}$	Total angular momentum
J	Total orbital-spin angular momentum quantum number
E_{HFS}	Hyperfine structure energy
a	Hyperfine structure constant
I	Nuclear spin angular momentum quantum number
F	Total angular momentum quantum number
$\mathbf{H}$	Hamiltonian operator
α	Magnetic hyperfine structure constant
β	Electric quadrupole interaction constant
$n^{2S+1}L_J$	Spectroscopic notation
Rb	Rubidium
c	Speed of light
$\tilde{v}$	Characteristic thermal velocity of atoms
k_B	Boltzmann constant
T	Temperature in Kelvin
$S_{3D}(v)$	Maxwell-Boltzmann distribution in 3D
$S_{1D}(v)$	Maxwell-Boltzmann distribution in 1D

M	Molecular weight of the gas
λ_0	Resonance wavelength
ν_o	Resonance frequency
ν	Frequency of laser
$\delta\nu_D$	Doppler linewidth
V_z	Speed of atoms in z-component
ν_L	Frequency seen by the moving atom
DFSAS	Doppler-Free Saturated-Absorption Spectroscopy
I_{probe}	Intensity of probe beam
I_{pump}	Intensity of pump beam
I_{sat}	Saturation intensity
Γ	Natural linewidth
h	Planck's constant
ν'	Cross-over resonance frequency
$\nu_{FF'}$	Frequency of transition $F \rightarrow F'$
$\mathbf{T}$	Kinetic energy operator
$\mathbf{p}_n$	Momentum of nucleus

$\mathbf{p}_i$	Momentum of the *i*th electron
$E(M)$	Energy level for an atom whose nucleus has a finite mass
$E(\infty)$	Energy level for an atom whose nucleus is infinitely heavy
$\delta(\Delta E)$	Energy difference
$\delta\tilde{\nu}$	Wavenumber difference
$\tilde{\nu}$	Wavenumber
δM	Isotope nuclear mass difference
r_0	Bohr’s radius
A	Mass number
ψ	Wave function
PZT	Piezoelectric transducer
ISO	Optical isolator
BS	Beam splitter
PBS	Polarizing beam splitter
PD	Photodiode
λ/2	Half-wave plate

CHAPTER 1

INTRODUCTION

1.1 Motivation and Background

There are several ways to probe and understand the fundamental concepts of physical phenomena. One of them is reproducing a pronounced extraordinary circumstance to comprehend its underlying principles and physical interpretation. We believe that when there are many techniques capable of investigating the same phenomenon, one of them tends to lead our understanding of physical reality to a more fundamental way. Deliberately performing absorption spectra that reflect the well-studied hyperfine structure of rubidium atoms provides an opportunity to implement inventive schemes which could lead to novel techniques and developments in atomic, molecular and optical (AMO) physics of which the key success is mainly dependent on the laser spectroscopy.

The advent of laser has revolutionized precision optical spectroscopy. When equipped with regulative tunability and high stability, unprecedented controls over sub-nanostructure would have made previously-unattainable experimental conditions possible. It has helped to transform traditional AMO, i.e., collisions and spectroscopy, to a new era of modern AMO science that has been revolutionizing experimental concepts and shedding light on long unsolved physical problems. Accordingly, the investigations over atomic energy structure that were only barely viable with conventional light sources can be readily performed.

To investigate the energy splitting of atomic gases, saturation spectroscopy is commonly employed. Generally, optical spectra are classified into two types related to either absorption or emission process. Each spectrum line represents one electronic dipole transition that can be specified with one resonant optical frequency. The energy-time uncertainty principle places a measurement limit to not to linewidth of the spectrum profile better than the natural bandwidth which is several magnitudes smaller than the dipole transition frequency (The dipole transition frequencies for rubidium D_1 and D_2 lines are about 2 THz while the natural linewidth for an absorption peak is around 30 MHz.). Hence, both absorption and emission lines should appear relatively sharp.

Experimentally, it is well known that observed spectrum lines demonstrate finite breadth which is independent of any optical system used to study them. In general, the Doppler effect, where random atomic motion causes selective absorptions of photons, plays a principle role. For rubidium at room temperature, the Doppler effect spreads the linewidth to about half an order of magnitude and thus smears the true nature of atomic transitions.

To pinpoint the resonant precisely to the atomic hyperfine structure, techniques such as Doppler-free saturated absorption spectroscopy [2] must be applied in order to resolve the broadened spectral profile. In addition, the Doppler-free spectroscopic routine will be a key ingredient in cooling and trapping of neutral atoms for various research aspects conducted in the Quantum-Atom Optics (QAO) laboratory, Chiang Mai University.

1.2 Outline of Thesis

In Chapter 2, necessary theories related to the experiment were provided briefly. This chapter starts with a concept of diode lasers and external cavity diode lasers that were used as optical sources in the experiment. Next, theories concerning atomic fine and hyperfine structure were explained along with the actual atomic structure of rubidium. Definitely, the principle of the Doppler-free saturated absorption spectroscopy, a spectroscopic technique that was conducted in this research was described. The calculations related to this chapter were shown in Appendix A and Appendix D.

In Chapter 3, the details of experimental setups including tuning of the external cavity diode laser and an optical schematic of the Doppler-free saturated absorption spectroscopy of rubidium were presented. Extra details of the method for tuning the external cavity diode laser and the list of all equipment used in this work were shown in Appendix B and Appendix E, respectively. Two schematics setups of the saturated absorption spectroscopy with different geometry are demonstrated and explained.

In Chapter 4, the experimental results and discussions were presented. The obtained absorption profiles with the Doppler broadening and the Doppler-free profile of the hyperfine spectra of rubidium were illustrated. At the end of the chapter, the width of the absorption spectra was analyzed, the separation in frequencies of the hyperfine structure was carried out, and both cases were compared against the theoretical values.

In Chapter 5, the conclusion and future plans of research were provided.

CHAPTER 2

THEORY

In this chapter, the principles of diode laser, the external cavity diode laser, and atomic spectroscopy theoretical background are described. First, the principle of diode laser is provided. Then, the external cavity diode laser (ECDL) is build up from advantages of the diode laser. After that, the theoretical background of atomic structure and atomic specie used in this work are introduced. Next, the broadened behavior of spectrum line is explained. Finally, the spectroscopic technique that used for reducing the broadening of the spectrum line is illustrated.

2.1 Diode Lasers

Diode lasers are electrically pumped semiconductor lasers. Their gain is generated by an electrical current flowing through a P–N or a P–I–N junction. Spontaneous emission pumped electrons simultaneously and randomly hops to states in the valence band and emitted photons gives out laser with a narrow bandwidth.

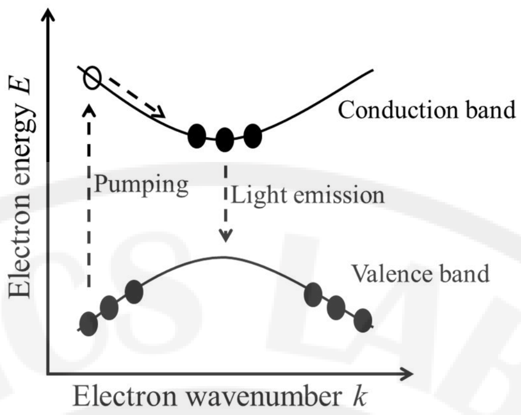

Figure 1 Excitation of electrons and light emission for a semiconductor.

Besides the spontaneous emission process, stimulated photoemission by incident photons through an optical feedback in a laser resonator leads to optical amplification. Without pumping, most of the electrons are in the valence band. These electrons near the band-top may be excited by a pump beam with photon energy slightly above the band-gap energy (smallest separation of the two bands) into the conduction band and then quickly decay to states near the bottom of the conduction band where the energies are lower. Simultaneously, the holes generated in the valence band move to the top of the band. Electrons excited across the junction recombine with holes and release the energy quanta as photons with energy roughly equivalent to the band-gap energy. The wider the curves near the top (bottom) of the valence (conduction) band, the smaller linewidth the laser processes. In addition, the light from the diode laser is emitted over a range of wavelengths near the intensity peak. This peak may be appreciably shifted to a particular wavelength by controlling the supplied current to the diode and stabilizing the operating temperature.

The edge-emitting lasers are the original and will be used in this work. The resonator length is typically between a few hundred micrometers and a few millimeters and will generate great loss if either end face of the resonator is not coated to prevent transmission. The laser beam is restricted to a waveguide structure using a double heterostructure, where the confined carriers may be represented by standing waves at selective frequencies and yielding an infinite set of discrete energies. Depending on the waveguide properties, its transverse dimensions, may offer a low threshold pump power and a high efficiency.

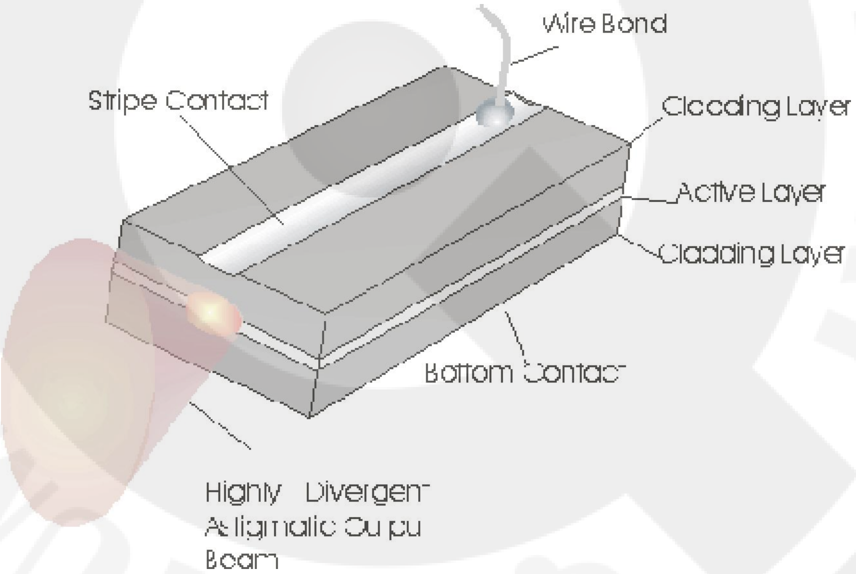

Figure 2 Schematic of the edge-emitting laser. The right edge is coated to obtain full reflection while the left edge where laser is emitted is anti-reflective coated [3].

Table 1 Emission wavelengths of various types of laser diodes [3].

Laser diode material (active region / substrate)	Typical emission wavelengths	Typical application
InGaN / GaN, SiC	380, 405, 450, 470 nm	data storage
AlGaInP / GaAs	635, 650, 670 nm	laser pointers, DVD players
AlGaAs / GaAs	720–850 nm	CD players, laser printers, pumping solid-state lasers
InGaAs / GaAs	900–1100 nm	pumping EDFAs and other fiber amplifiers; high-power VECSELs
InGaAsP / InP	1000–1650 nm	optical fiber communications

2.2 External Cavity Diode Laser (ECDL)

Diode lasers were used extensively in atomic physics spectroscopy because of their advantages, e.g., low cost in contrast to other types of lasers, narrow spectral width and that they do not require cooling to low temperature while operating. With suitable optical feedback, a typical bandwidth of a few nanometers resulting from the simultaneous oscillation of multiple longitudinal resonator modes may be reduced to a linewidth of few megahertz. This tunability of lasers has revolutionized optical spectroscopy [4]. Further linewidth narrowing can be achieved with narrow-band optical feedback from a reference external cavity.

An external-cavity diode laser plays an important role in laser spectroscopy particularly laser-atom cooling and trapping which requires tunability within sub-megahertz linewidth to moderate powers (order of 100 mW), a great spectral purity and extremely long-term stability. Practically, they are more convenient to use due to their insensitiveness to stray external light feedback in contrast to plain laser diodes. For a 780 nm diode laser as will be used in this work, when operating at its center frequency, the power output is most intense within the frequency range of $3.85\times10^{14}\pm1\times10^{6}\,\mathrm{Hz}$.

The part assembly for the ECDL may be classified into two configurations, the Littman–Metcalf [5] and the Littrow configurations for which the disadvantages are given in Table 2. The later arrangement with fixed direction output beam [6] will be employed in this research to attain high intensity beam. All major components, which are a diode laser, a collimating lens and a diffraction grating as the end mirror of the external resonator, are indicated in Figure 3.

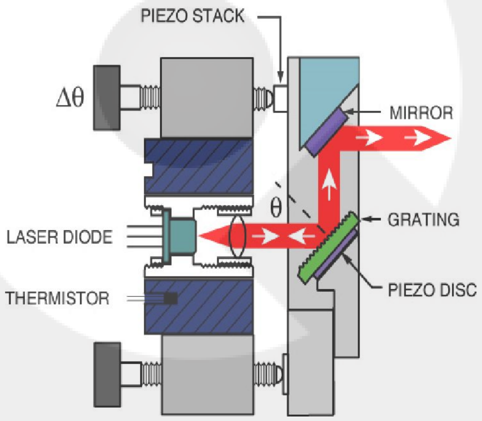

Figure 3 Schematic diagram of an external cavity diode laser designs in the Littrow configuration [6].

Table 2 Advantages and drawbacks of each ECDL configuration [7].

Configuration	Advantage	Disadvantage
Littrow configuration	First-order diffracted beam provides an optical feedback to the laser diode chip and the strong zeroth-order diffracted beam is the output.	While emission wavelength is being tuned by rotating the diffraction grating, direction of the output beam changes accordingly. This is impractical.
Littman-Metcalf configuration	Fixed direction of the output beam and smaller line-width as the wavelength-dependent diffraction occurs twice for one resonating circle.	Lower output power since the zero-order reflection of the beam reflected by the tuning mirror is lost.

In the Littrow configuration, the grating is aligned such that the first-order diffracted beam is directed to the diode laser (as optical feedback) and that the zeroth order diffracted beam, the most intense one, is used as an output. The diffraction grating used in this configuration is blazed and reflection-type grating so that we may choose the grating which respond most efficiently to transition frequencies of rubidium atoms. Assuming that all the slits are identical under the Fraunhofer conditions, the light curve of a multiple slit arrangement will be the interference pattern multiplied by the single slit diffraction envelope. The diffraction pattern from the grating is governed by the grating equation,

$$d\left(\sin\theta_i + \sin\varphi_m\right) = m\lambda, \tag{1}$$

where d is the groove spacing (pitch), θ_i is the incident angle, and φ_m is the diffracted angle of the mth order.

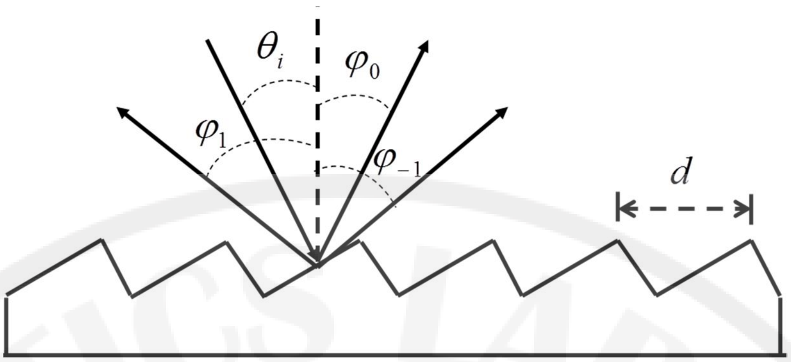

Figure 4 Schematic diagram of a blazed reflection grating.

For geometrical wave diffraction, the incident and the diffraction angle are equal so that the grating Equation (1) becomes

$$\lambda = 2d\sin\theta_i . \tag{2}$$

According to Equation (2), the wavelength of the laser light can be tuned by altering the diffraction grating angle. The horizontal and vertical angle of the grating can be finely adjusted via an applied current to the piezoelectric disk as shown in Figure 3.

A narrow linewidth and tunability of the diode laser with an addition of an external cavity, a precision temperature control and a supplied current is achieved because the laser diode can be forced to operate a single mode with a very narrow linewidth (less that 1 MHz) [8] by an optical feedback that is the first order diffracted beam in to the diode. External cavities take advantage of the fact that the laser diode is highly sensitive to the optical feedback. An external wavelength selective element is used to provide the optical feedback to diode and control its operating wavelength. Hence, there are three major components of the ECDL to tune emitted laser wavelength from the diode. First, the diode laser is used to produce laser light of the system. Second, the emitted laser light is collimated by collimating lens tube. Third, diffraction grating is used as wavelength selective element.

For the diffraction grating is a blazed grating (Littrow grating), the angle and groove spacing or specification of the grating can be determined. In order to obtain our desire wavelength, i.e., for 780 nm laser light we need at least 1,800 lines per mm groove spacing of the grating with incident angle of 45 degree to send the first order diffracted beam back to the diode (see Appendix 1 for calculation). The optical feedback into the diode forces it to operate at the wavelength of the feedback [8].

2.3 The Theory of Atomic Fine and Hyperfine Structure

Atoms have different forms of angular momentum contributing to the total angular momentum such as an orbital angular momentum, a spin angular momentum of the electrons and of the nucleus. All angular momenta generate magnetic moments interacting with each other. The following is a brief summary of an atomic structure [9-11].

2.3.1 Magnetic Moment of Orbital Angular Momentum

Classically, the magnetic moment of the angular momentum can be understood from a circular current generated by electrons' orbit around the nucleus. The magnetic dipole moment can be expressed as

$$\boldsymbol{\mu}_{\mathbf{L}} = -\frac{g_L \mu_B}{\hbar}\mathbf{L}, \tag{3}$$

where $g_L = 1$ is the magnetogyric ratio of the orbital magnetic moment, μ_B is Bohr's magnetron, and $\mathbf{L}$ is the orbital angular momentum of the electrons. The vector of an orbital magnetic moment is antiparallel to the vector of the orbital angular momentum. It is quantized and can be determined only in magnitude and z-component at the same time.

2.3.2 Magnetic Moment of Spin Angular Momentum

The following magnetic moment is correlated to spin angular momentum ($\mathbf{S}$),

$$\boldsymbol{\mu}_{\mathbf{S}} = -\frac{g_S \mu_B}{\hbar}\mathbf{S}. \tag{4}$$

The important difference to the magnetic moment generated by the orbital angular momentum is the difference in the magnetogyric ratio, $g_S \approx 2$.

Both magnetic moments $\boldsymbol{\mu}_{\mathbf{L}}$ and $\boldsymbol{\mu}_{\mathbf{S}}$ combine to give a total magnetic moment that is a fine structure interaction, so called LS-coupling:

$$\boldsymbol{\mu}_{\mathbf{J}} = -\frac{g_J \mu_B}{\hbar}\mathbf{J}, \tag{5}$$

where $\mathbf{J}$ is an orbital-spin angular momentum and g_J is a Landè factor given by

$$g_J = 1 + \frac{J(J+1) + S(S+1) - L(L-1)}{2J(J+1)}. \tag{6}$$

2.3.3 Magnetic Moment of Nuclear Spin Angular Momentum

Atomic nuclei possess a nuclear spin angular momentum **I** with $|\mathbf{I}| = \sqrt{I(I+1)}\hbar$. The correlation between the nuclear spin and a nuclear magnetic moment is

$$\boldsymbol{\mu}_\mathrm{I} = -\frac{g_I \mu_N}{\hbar}\mathbf{I}\,, \tag{7}$$

and

$$\mu_N = \frac{e\hbar}{2m_P} \tag{8}$$

is the nuclear magnetron, where m_P is the proton mass. The nuclear magnetron is smaller than the Bohr magnetron by the ratio of electron and proton mass, $\mu_N = \mu_B / 1836$.

2.3.4 Fine and Hyperfine Interaction

Atomic fine structure splitting is a result of the LS-coupling of an bound electron in an atom. The energy associated with the coupling is described by

$$\begin{aligned} E_{L,S} &= -\boldsymbol{\mu}_\mathrm{S} \cdot \mathbf{B}_\mathrm{L} \\ &= \frac{a^*}{2}\left[J(J+1) - L(L+1) - S(S+1)\right], \end{aligned} \tag{9}$$

where the expression of a^* for atoms similar to hydrogen is (with n principal quantum number)

$$a^{*} \propto \frac{Z^{4}}{n^{3}L(L+\frac{1}{2})(L+1)}. \tag{10}$$

The hyperfine interaction energy can be calculated in an analogous way to the fine structure energy. It is three orders of magnitude smaller than the fine structure interaction energy described above as a result of the ratio of the nuclei magnetic moment to that of electrons, which is approximately 1/1836.

At the nucleus, a magnetic field $\mathbf{B_J}$ is generated by an orbital motion and spin of the electrons. This field influences the magnetic moment of the nucleus and, therefore, the orbital-spin angular momentum of the electrons, $\mathbf{J}$, couple with that of the nucleus, $\mathbf{I}$, into a total angular momentum, $\mathbf{F}$. In analogous to the LS-coupling of the electrons, the coupling of the nuclear spin angular momentum with the orbital-spin angular momentum form the total angular momentum,

$$\mathbf{F} = \mathbf{J} + \mathbf{I}, \tag{11}$$

where the magnitude of total angular momentum is

$$|\mathbf{F}| = \sqrt{F(F+1)}\hbar. \tag{12}$$

The quantum number of total angular momentum $\mathbf{F}$ can have the values

$$|J-I| \leq F \leq |J+I| \tag{13}$$

Thus, there are $(2I+1)$ or $(2J+1)$ possibility, depending on whether I is smaller or larger than J. It is worth nothing, that J and I determine the number of hyperfine levels. Experimentally, once the number of hyperfine levels is counted, the nuclear spin, $\mathbf{I}$, can be determined readily given that $\mathbf{J}$ is known. The interaction energy is

$$\begin{aligned} E_{HFS} &= -\boldsymbol{\mu}_{\mathbf{I}} \cdot \mathbf{B}_{\mathbf{J}} \\ &= \frac{a}{2}\left[F(F+1) - I(I+1) - J(J+1)\right]. \end{aligned} \tag{14}$$

Here a is a hyperfine structure constant,

$$a = \frac{g_I \mu_N B_J}{\sqrt{J(J+1)}}. \tag{15}$$

The energy hyperfine structure is proportional to the F values of the total angular momentum when the values of I and J are fixed. Thus, the energy interval between adjacent F levels is

$$\Delta E_{HFS} = E_F - E_{F-1} = aF. \tag{16}$$

This is called the interval rule or the Landè interval rule for the hyperfine structure.

The Hamiltonian for an isolated atom having a single electron may be expressed as

$$\begin{aligned} \mathbf{H} = &-\frac{\hbar^2}{2m}\nabla^2 - \frac{Z_{eff}e^2}{4\pi\varepsilon_o r} + \zeta(r)\mathbf{L}\cdot\mathbf{S} + \alpha\mathbf{J}\cdot\mathbf{I} \\ &+ \frac{\beta}{2I(2I-1)2J(2J-1)}\left[3(\mathbf{I}\cdot\mathbf{J})^2 + \frac{3}{2}(\mathbf{I}\cdot\mathbf{J}) - I(I+1)J(J+1)\right]. \end{aligned} \tag{17}$$

The constants α and β are for the magnetic hyperfine structure (relevant to the magnetic hyperfine interaction which is the negative product of the nuclear magnetic dipole moment and the magnetic field produced at the nucleus by an electron,

$-\boldsymbol{\mu}_n \cdot \mathbf{B}_e$) and the electric quadrupole interaction in the unit of energy. Bold letters stand for operators whereas the non-bold letters are for the quantum number corresponding to each angular momentum mentioned. In addition, the relativistic correction is exclusive and the spherical symmetric potential (central field approximation) is assumed. The Hamiltonian in Equation (17) consists of five terms. They are kinetic energy (**K**), effective Coulombic potential (**V**) due to nuclear electric monopole, the fine structure spin-orbit coupling ($\mathbf{H}_{SO}$), the magnetic hyperfine interaction, and the electric quadrupole hyperfine interaction, respectively. The expressions

$$\mathbf{L}\cdot\mathbf{S} = \frac{\hbar^2}{2}\left[J(J+1) - \ell(\ell+1) - s(s+1)\right] \tag{18}$$

and

$$\mathbf{J}\cdot\mathbf{I} = \frac{1}{2}\left[F(F+1) - J(J+1) - I(I+1)\right] = \frac{1}{2}C \tag{19}$$

for $\mathbf{J} = \mathbf{L} + \mathbf{S}$ and $\mathbf{F} = \mathbf{J} + \mathbf{I}$ allow the energy to be rewritten as

$$E_{J,F} = E_J + \alpha\frac{C}{2} + \beta\frac{\frac{3}{4}C(C+1) - I(I+1)J(J+1)}{2I(2I-1)J(2J-1)}, \tag{20}$$

where E_J is the energy for the state $n^{2S+1}L_J$. The optical transitions in the hyperfine structure must satisfy the atomic transition selection rules,

$$\Delta s = 0,\ \Delta J = 0, \pm 1 \text{ and } \Delta F = 0, \pm 1 \text{ for } 0 \not\to 0. \tag{21}$$

2.4 Rubidium

In this work, we aim to study the hyperfine structure of rubidium atoms. There are several reasons for using rubidium. Firstly, optical transitions in rubidium are easily accessible by commonly available diode lasers. Rubidium also has an energy level structure allowing a simple optical pumping scheme to be employed for the labeling and detection. Additionally, rubidium has only one outer shell electron, making it similar in nature to hydrogen, so its behavior is relatively well understood theoretically [8], [12].

Rubidium is an alkali element which is a soft, silvery metal, and one of the most active chemical elements. Rubidium has 37 electrons, one being a valence electron and its electronic configuration can be written as

$$1s^2;2s^2;2p^6;3s^2;3p^6;3d^{10};4s^2;4p^6;5s^1.$$

There is one valence electron in the shell $n=5$, s-orbital. The s-orbital represents electron orbital angular momentum $L=0$. The valence electron has the electron spin angular momentum $S=1/2$. Thus the total electron angular momentum can be determined as

$$J=L+S=0+\frac{1}{2}=\frac{1}{2}.$$

The term symbol of rubidium would be represented by the spectroscopic notation, $n^{2S+1}L_J$, as $5\,^2S_{1/2}$ for the ground term (ground state) of the fine structure.

If the valence electron is excited into the first excited state $(L=1)$, the term symbol can be determined similarly to the ground term. In the first excited state, the total electron angular momentum is

$$J = L + S = 1 + \frac{1}{2} = \frac{3}{2}, \frac{1}{2}.$$

The term symbol of the first excited states is $5\,^{2}P_{1/2}$ and $5\,^{2}P_{3/2}$.

The term symbol as mentioned above is generally used for the atomic fine structure. However, it can be also applied to the atomic hyperfine structure by putting the total angular momentum F as a subscript in front of the electron angular momentum, $n\,^{2S+1}_{F}L_J$.

There are two natural abundant isotopes of rubidium, ^{85}Rb (≈72.15%), and ^{87}Rb (≈27.85%). Each isotope has its nuclear spin angular momentum $I = \frac{5}{2}, \frac{3}{2}$ for ^{85}Rb and ^{87}Rb, respectively. The total angular momentum (ground state) for both isotopes can be defined respectively as

$$F = I + J = \frac{5}{2} + \frac{1}{2} = 3, 2$$

and

$$F = I + J = \frac{3}{2} + \frac{1}{2} = 2, 1.$$

In the first excited state of rubidium, the total angular momentum for each isotope will be obtained as shown in Table 3.

Table 3 Total angular momentum of the first excited state of rubidium.

	I	J	$F = I+J$
^{85}Rb	$\frac{5}{2}$	$\frac{3}{2}$	4, 3, 2, 1
		$\frac{1}{2}$	3, 2
^{87}Rb	$\frac{3}{2}$	$\frac{3}{2}$	3, 2, 1, 0
		$\frac{1}{2}$	2, 1

At this point, the term symbol of the fine and hyperfine state for the ground and the first excited state of rubidium is identified. By applying the Hund's rules and the interval rule, the Grotrian diagram or the energy level diagram for these two states can be constructed as shown in Figure 5. The electronic transition in both fine and hyperfine structure must satisfy the atomic transition selection rule, Equation (21).

According to the splitting of the fine structure energy levels, rubidium has two D line transitions named D_1 ($5^2S_{1/2}$-$5^2P_{1/2}$) at 795 nm, and D_2 ($5^2S_{1/2}$-$5^2P_{3/2}$) at 780 nm, respectively. The atomic selection rule presents the D_2 transition line at 780 nm has four absorption peaks corresponding to the fine structure (Figure 6). Two peaks belong to ^{85}Rb and two to ^{87}Rb. The coupling between the nuclear angular momentum with the total electron angular momentum to form the total angular momentum causes the hyperfine structure. The hyperfine structure energy in the ground and the excited state of rubidium for the D_2 line transition, that can be obtained from [13-14], is tabulated in Table 4 as well as the interval rule, Equation (16). For the D_2 line transition, the hyperfine levels (absorption) are labeled in Figure 5, and the transition energy and relative absorption intensity between the hyperfine states is tabulated in

Table 5. The relative intensity of the hyperfine state transition can be obtained from the relative intensity tables for spectrum lines [15]. The absorption spectrum with relative intensity is also depicted in Figure 7, and the label on each spectrum line is associated with the name of the spectrum in Table 5.

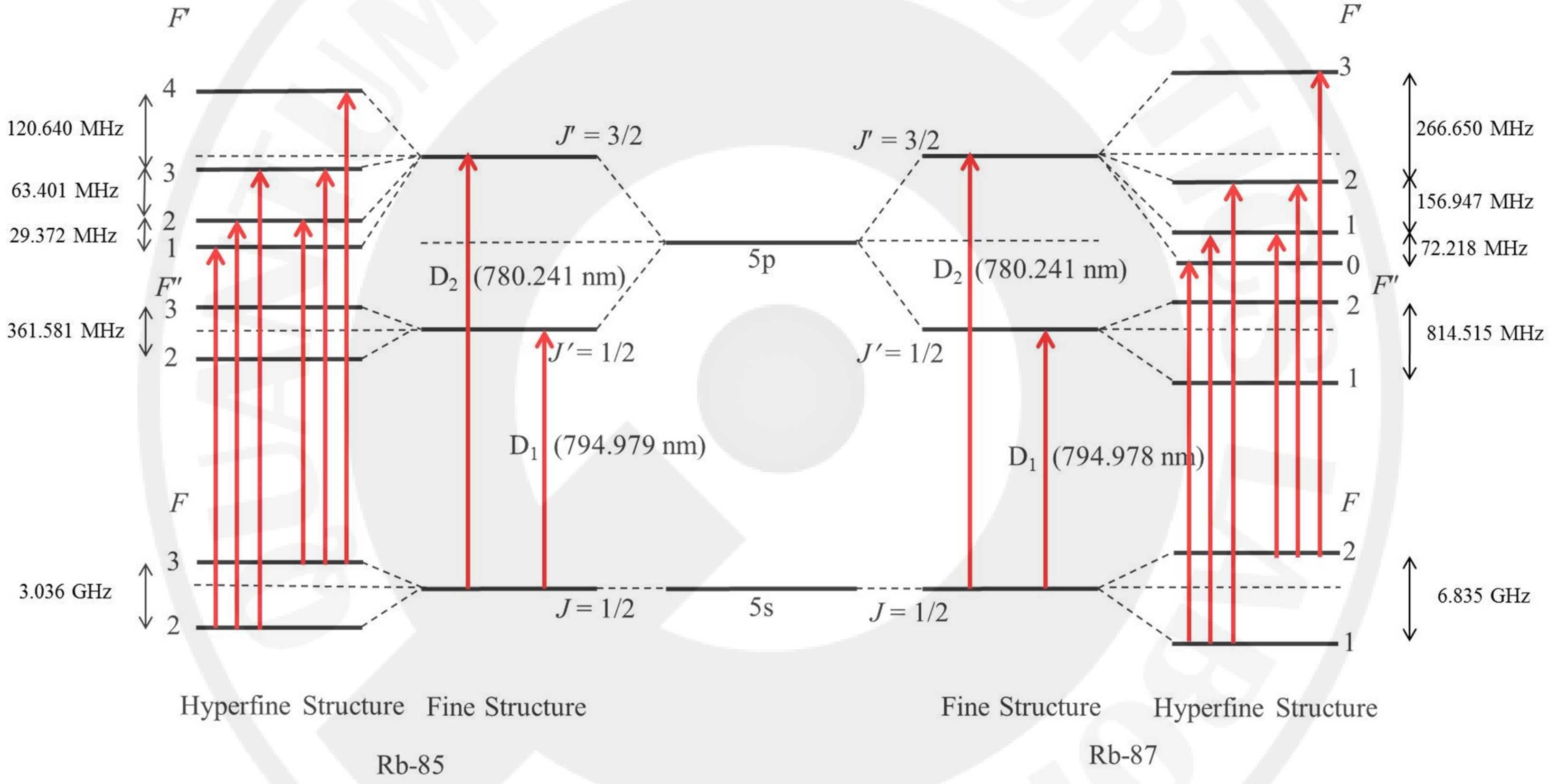

Figure 5 Fine and hyperfine structure of rubidium and absorption transition of D_2 line in the hyperfine structure. (NOT TO SCALE) The dashed line at 5s level is a neutral line of the fine structure.

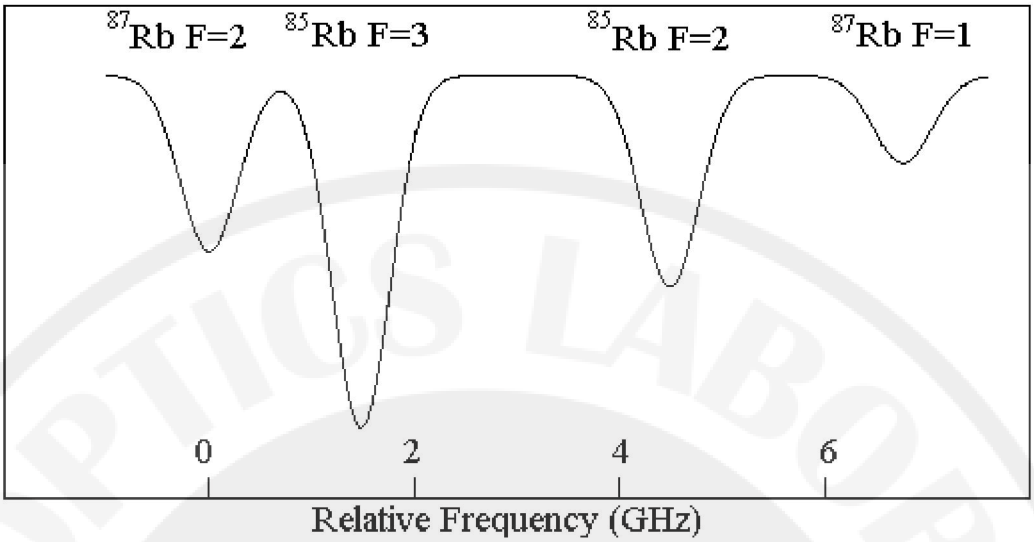

Figure 6 Relative frequency spacing with increasing frequency of the fine structure lines [16].

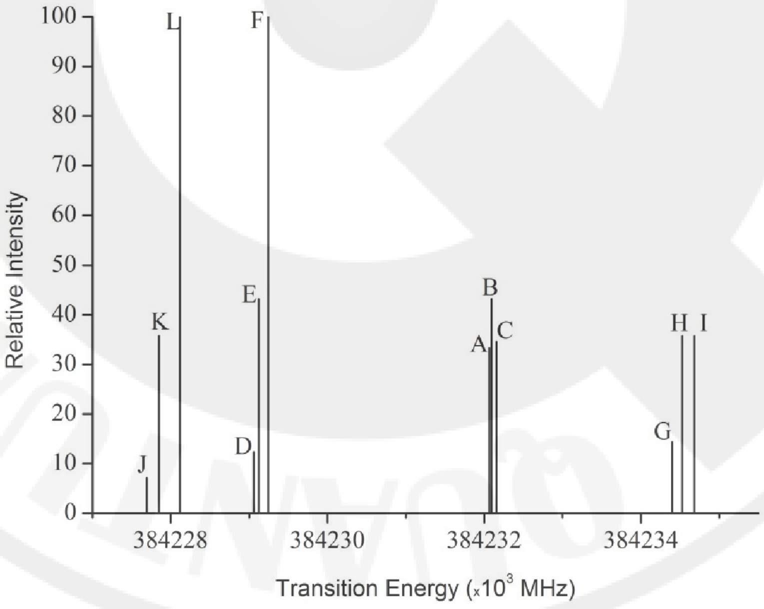

Figure 7 Absorption spectrum with relative intensity of the D_2 line of ^{85}Rb and ^{87}Rb.

Table 4 The hyperfine structure energy in the ground and the excited state of rubidium.

Isotope	*F*		Energy (MHz)	E_{cal}	ΔE_{cal}	ΔE (MHz)	Interval
^{85}Rb	$J = 3/2$	4	384230506.578	$\frac{15}{4}a'$	$4a'$	120.640	4:3:2
		3	384230385.938	$-\frac{1}{4}a'$	$3a'$	63.401	
		2	384230322.537	$-\frac{13}{4}a'$	$2a'$	29.273	
		1	384230293.165	$-\frac{21}{4}a'$			
	$J = 1/2$	3	1264.888	$\frac{5}{4}a''$	$3a''$	3035.732	-
		2	-1770.843	$-\frac{7}{4}a''$			
^{87}Rb	$J = 3/2$	3	384230678.208	$\frac{9}{4}a'$	$3a'$	266.650	3:2:1
		2	384230411.558	$-\frac{3}{4}a'$	$2a'$	156.947	
		1	384230254.611	$-\frac{11}{4}a'$	$1a'$	72.218	
		0	384230182.393	$-\frac{15}{4}a'$			
	$J = 1/2$	2	2561.005	$\frac{3}{2}a''$	$2a''$	6832.681	-
		1	-4271.676	$-\frac{5}{4}a''$			

Table 5 Transition energy and relative intensity of the D_2 line transition of rubidium.

Transition $F \rightarrow F'$		**Initial State Energy (MHz)**	**Final State Energy (MHz)**	**Transition Energy (MHz)**	**Line**	**Relative Intensity**
^{85}Rb	2→1	-1770.843	384230293.165	384232064.008	A	33.3
	2→2	-1770.843	384230322.537	384232093.338	B	43.2
	2→3	-1770.843	384230385.938	384232156.781	C	34.6
	3→2	1264.888	384230322.537	384229057.649	D	12.3
	3→3	1264.888	384230385.938	384229121.050	E	43.2
	3→4	1264.888	384230506.578	384229241.690	F	100
^{87}Rb	1→0	-4271.676	384230128.393	384234400.069	G	14.3
	1→1	-4271.676	384230254.611	384234526.287	H	35.7
	1→2	-4271.676	384230411.558	384234683.234	I	35.7
	2→1	2561.005	384230254.611	384227693.606	J	7.1
	2→2	2561.005	384230411.558	384227850.553	K	35.7
	2→3	2561.005	384230678.208	384228117.203	L	100

2.5 Spectral Line Broadening (Doppler Broadening)

Theoretical recognizability of an absorption spectrum, a fingerprint that can be used to identify the atoms, elements, or molecules [17], gets diminished with increasing dispersion of non-apparent spectroscopic transitions. Typical absorption profiles are greatly influent by various types of broadening mechanisms. Some of them such as natural, collisional and power broadening are homogeneous and hence are responsible for the Lorentzian spectral lineshape. The other inhomogeneous mechanisms, frequently referred to the Doppler Effect, will give a Gaussian intensity profile. The combination of Lorentzian and Gaussian outlined views can be approximated by a Voigt profile [18].

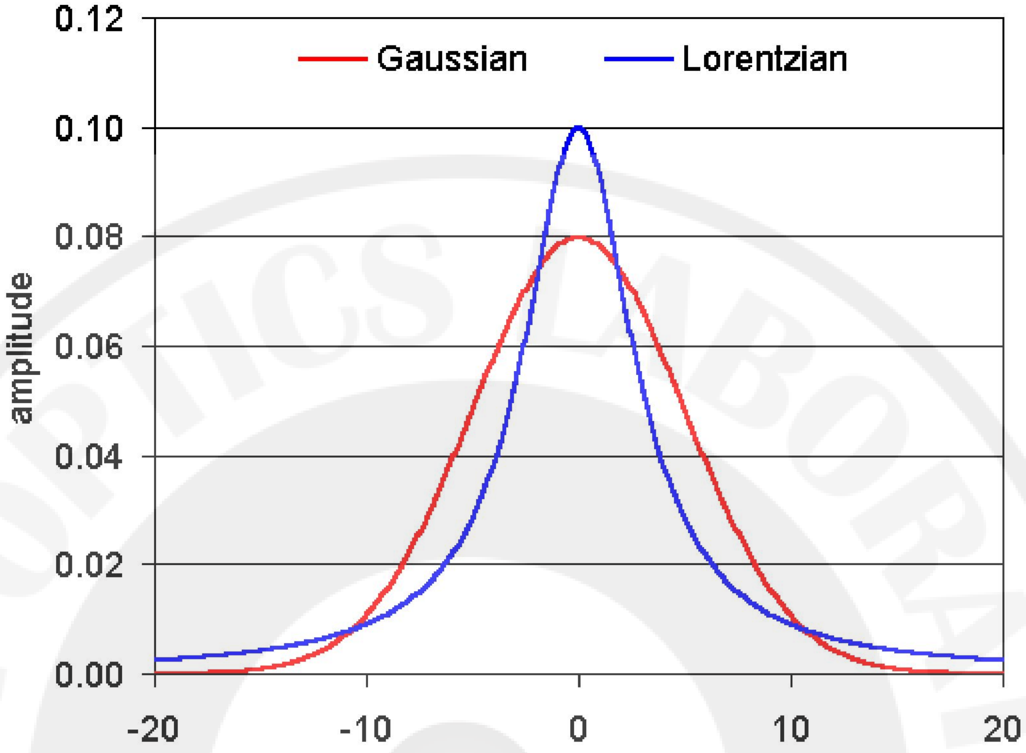

Figure 8 Gaussian and Lorentzian spectral lineshapes [17].

The homogeneous broadening, we can briefly describe each type as follows. The natural linewidth arises from the energy levels of atoms that are not infinitely sharp. Due to the Heisenberg's uncertainty principle, electron remains there in the excited state for an average time Δt before decaying to the ground state. A photon emitted in a transition from the excited state to the ground state will have a range of possible frequencies. For the collision broadening (also called pressure broadening), atoms collide frequently in a dense gas. Collisions will randomize the phase of the emitted radiation. If the collisions are frequent enough, they will shorten the life time of the excited states. The short life time leads to an increase in the lindwidth that depends on the collision rate. Another type of the homogeneous mechanism, power broadening, is an effect where the linewidth of a laser is broadened by the laser itself. Higher laser intensity leads to a larger linewidth, and it reduces the life time of the excited states due to the stimulated emission.

In this section, we take into account the inhomogeneous type especially the Doppler broadening that can be removed from the observed spectrum profile, leaving only the profile without the Doppler lineshape.

The Doppler effect refers to the frequency shift of observed electromagnetic wave due to atomic motion along the wave’s propagation direction. This effect is central to spectroscopy as well as laser cooling processes. Given light propagating in the z-direction and atom’s velocity (nonrelativistic) as $\vec{v}$,

$$\nu_{absorbed} = \nu_{emitted}\left(1-\frac{\vec{v}\cdot\hat{z}}{c}\right). \tag{22}$$

The usual terminology is to refer to the absorbed light as blue- or red-shift in the reference frame of the atom; the blue-shifted light associates with a positive shift in the frequency and energy, and vice versa for the red-shifted light.

Let us look briefly at the velocity distributions present in a cloud of atomic gas. There are two ways to view the distribution of atomic velocities; the velocity of atoms along one specific direction (orthogonal velocities count as zero along the direction of interest, Figure 10) and the velocity of atoms in any given direction (spherical, integrating all velocities as positive, Figure 9). Let

$$\tilde{v} \equiv \sqrt{k_B T / M} \tag{23}$$

the characteristic thermal velocity of atoms, based on temperature. The Maxwell-Boltzmann distribution is given by

$$S_{3D}(v) = \sqrt{\frac{2}{\pi}}\frac{v^2}{\tilde{v}^2}\exp\left(-\frac{v^2}{2\tilde{v}^2}\right) \tag{24}$$

$$S_{1D}(v) = \frac{1}{\sqrt{2\pi}\tilde{v}}\exp\left(-\frac{v_x^2}{2\tilde{v}^2}\right) \tag{25}$$

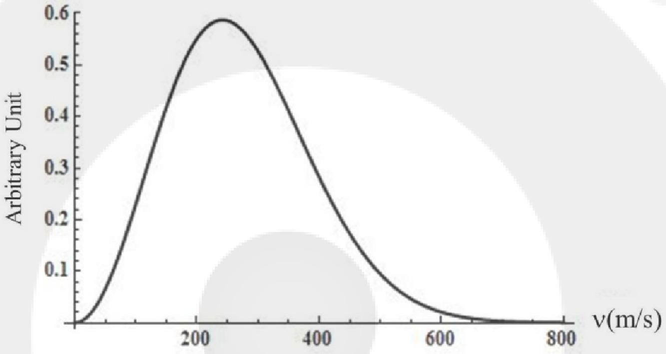

Figure 9 The 3D Maxwell-Boltzmann speed distributions for ^{85}Rb atoms at room temperature.

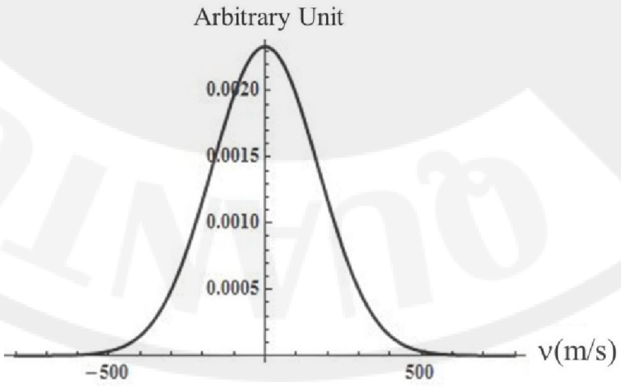

Figure 10 The 1D Maxwell-Boltzmann speed distributions for ^{85}Rb atoms at room temperature.

The idea of moving atoms is significant to Doppler-free spectroscopy. The stochastic thermal motion of atoms leads to the inhomogeneous spectral broadening via the Doppler shift, some atoms absorb the red-shifted light and some absorb the blue-shifted light. Putting the one-dimensional Maxwell-Boltzmann distribution together with the Doppler shift yields the lineshape function for the Doppler broadening. Taking T as the gas temperature in Kelvin, M as the molecular weight of the gas and λ_o as the wavelength in Å, one obtains [19]

$$S(v) = \frac{1}{\delta v_D}\left(\frac{4\ln 2}{\pi}\right)^{1/2} e^{-4\ln 2(v-v_o)^2/\delta v_D^2}\ \frac{1}{\mathrm{MHz}}, \tag{26}$$

$$\delta v_D = 2.15\times 10^6\left[\frac{1}{\lambda_o}\left(\frac{T}{M}\right)^{1/2}\right]\mathrm{MHz}, \tag{27}$$

where δv_D is the Doppler linewidth. Substituting in the values for Rubidium atoms at room temperature,

$$\delta v_D = 2.15\times 10^6\left[\frac{1}{7806\,\mathrm{\mathring{A}}}\left(\frac{298\mathrm{K}}{85.5g}\right)^{1/2}\right]\approx 514\ \mathrm{MHz}. \tag{28}$$

The calculation yields the width for the transition of room temperature atoms as measured by one directed beam. The linewidth of the transition to which we must stabilize is roughly 2π·6 MHz (≈40 MHz). While the Doppler broadening of a transition by hundreds of MHz seems severe, there are techniques such as saturation spectroscopy [20] to overcome this apparently inherent difficulty.

2.6 Doppler-free Saturated Absorption Spectroscopy

When the frequency of a diode laser is tuned close to an atomic transition frequency, randomly moving atoms absorb light with different frequencies due to the Doppler effect, which in our case is non-relativistic. According to the Doppler relation, Equation (22), for the atom having the z-component speed V_z, the frequency seen by the moving atom is

$$\nu_L = \nu_o \left(1 + V_z / c\right), \tag{29}$$

where ν_o is the laser frequency. The atom moving toward or away from a laser source locating on the z -axis will see the radiation blue or red shifted, respectively. Thus the true fine or hyperfine structure may be obtained only when the Doppler Effect is excluded [12].

A simple method to eliminate the Doppler broadening is the Doppler-Free Saturated-Absorption Spectroscopy (DFSAS). The non-linear absorption spectrum is obtained from a probe beam that interacts with the same group of optically pumped atoms (Figure 11b). It is then subtracted from the Doppler broadened absorption spectrum obtained from the linear spectroscopy (Figure 11a). This technique is employed to study the absorption lines with resolution beyond the Doppler linewidth. The structure of the hyperfine splitting will be used in the future project entitled: “Light Assisted Collision of Cold Atoms in an Optical Dipole Trap.” The experimental setup and theoretical discussion for the DFSAS are given as follows.

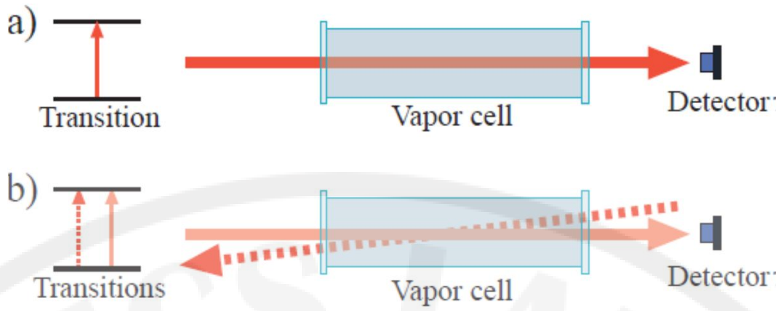

Figure 11 (a) Linear and (b) non-linear spectroscopy [21].

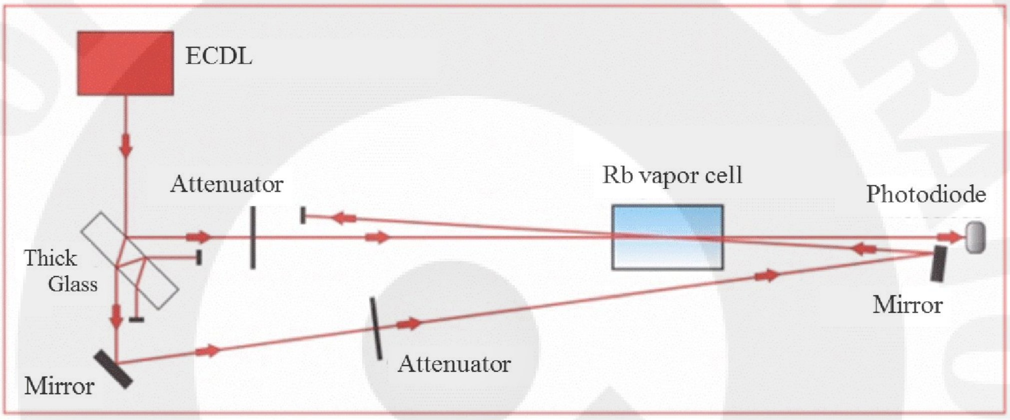

Figure 12 Optical arrangement for Doppler-free saturated absorption spectroscopy. The probe beam propagates to the right and overlaps the pump beam [17].

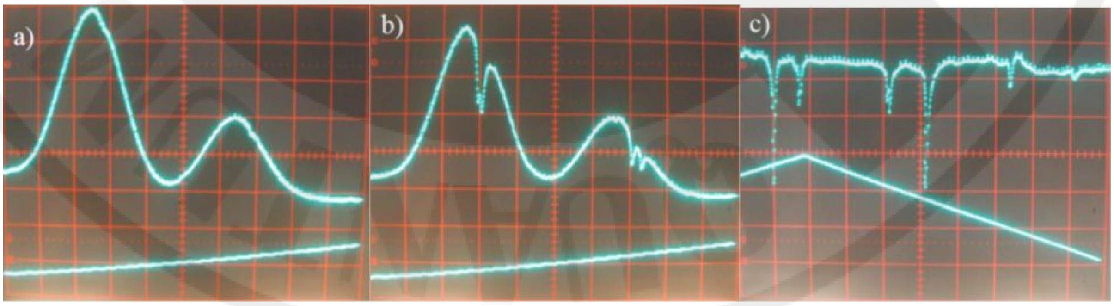

Figure 13 a) Doppler-broadened spectral lines b) Doppler-broadened spectral lines with hyperfine structure and c) Doppler-free saturated absorption spectral lines [21]. The diagonal line is the ramp current that used to drive the piezo disc.

A beam emitted from the ECDL is split into two probe beams and a pump beam with higher intensity. The direction of propagation of each beam is indicated by an arrow (Figure 12). When the piezoelectric plate in the ECDL is electrically driven, the frequency of the beam sweeps across transition lines $5^2S_{1/2} \rightarrow 5^2P_{3/2}$ of rubidium and the Doppler-broadened absorption spectrum is observed (Figure 13a). This happens because only atoms with particular velocity along the first probe beam path are in resonance with the beam. If the first probe beam is blocked as the frequency sweeps, the second beam will provide a nonlinear saturated absorption lines riding on the Doppler-broadened spectrum (Figure 13b) because the pump beam, or equivalent term: the saturated beam, continuously depopulates atoms in the intercept region that relatively at rest along the beam axis. In other word, these portion of energetic atoms may absorb photons from the two counter-propagating beams so that the field intensity at a photodiode drops exactly at hyperfine transition frequencies (some peaks are the crossover line) as shown by the downward peaks in Figure 13b. Wiring the two photodiodes in such way that signals from the two probe beams subtract, the hyperfine absorption lines can be directly monitored on an oscilloscope.

In laser spectroscopy, an atom may be treated as a two-level system. In the saturated absorption spectroscopy, the intense pump beam will cause most of atoms to be in the excited state; when the number of atoms in the ground state and the excited state are approximately equal, the transition is saturated. Normally, the conditions for the intensity of the probe and the pump beam are $I_{\mathrm{probe}} \ll I_{\mathrm{sat}}$ and $I_{\mathrm{pump}} \gg I_{\mathrm{sat}}$, respectively, where I_{probe} is the intensity of the probe beam, I_{pump} is the intensity of the pump beam, and I_{sat} is the saturation intensity. The saturation intensity is an intensity limit indicating the saturation of the transition in the spectroscopy. If the laser intensity is much greater than the saturation intensity, the transition will be saturated and the population is equally distributed between the ground and the excited state [19]. The value of the saturation intensity is given by

$$I_{\text{sat}} = \frac{2\pi^2 hc\Gamma}{3\lambda^3}, \tag{30}$$

where Γ is natural linewidth, h is Planck's constant, c is speed of light, and λ is laser wavelength. For the case of rubidium, the natural linewidth $\Gamma = 6.066618\,\text{MHz}$ [20, 22], giving the saturation intensity $I_{\text{sat}} = 1.67\,\text{mW/cm}^2$.

2.7 Cross-over Resonance

In a saturated absorption spectroscopy, the Doppler effect has an important role for producing extra peaks that are not corresponding to the atomic transition. The extra peaks arising from a result of atomic motion and counter propagating laser beams are called cross-over resonance. Suppose we divide atoms with same speed into two groups according to the direction of propagation along the laser axis. When the laser is tuned to the average frequency of the two transition frequencies that share a common ground state E_1, the first group of atoms resonances with the laser that appears blue-detuned. Similarly, the second groups get excited to E_3 by the same laser but arrived red-detuned. Hence, a cross-over peak emerge midway between two particular transitions [9] and contribute a dip twice as deep with respect to the two resonance peaks.

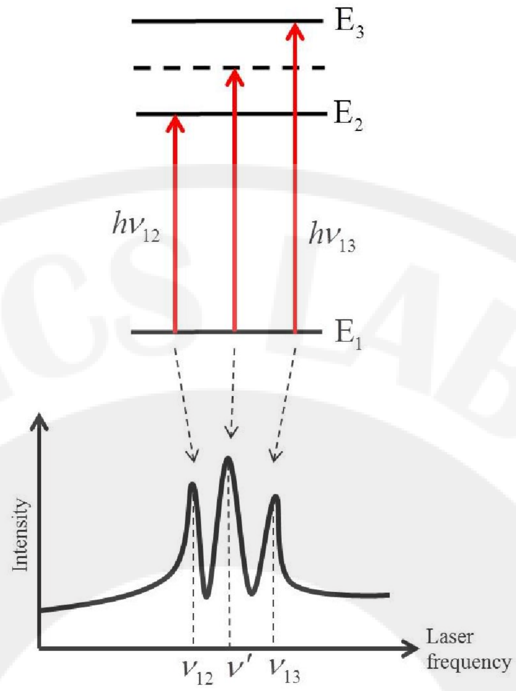

Figure 14 The formation of cross-over resonance. A three levels atom with two allowed transitions at frequencies ν_{12} and ν_{23}. A cross-over resonance occurs at ν', midway between two saturated absorption peaks corresponding to transitions at frequencies ν_{12} and ν_{23}.

For the D$_2$ line transition of rubidium, there should be three theoretical absorption peaks in the saturated absorption spectrum according to the selection rule. When the Doppler effect is inclusive, there will be six absorption peaks in the saturated absorption profile. Other three peaks are the cross-over resonance peaks. The value of the cross-over transition energies in each hyperfine state transition of rubidium are illustrated in Table 6 as well as the interval rule including the cross-over resonance peaks are shown in Table 7.

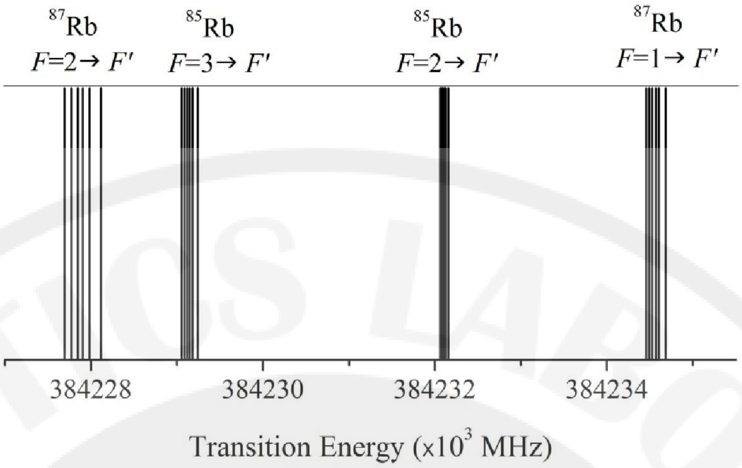

Figure 15 Hyperfine absorption spectrum with cross-over resonances of the D_2 line of ^{85}Rb and ^{87}Rb.

Table 6 Transition energies in hyperfine states with cross-over resonance of the D_2 line transitions of ^{85}Rb and ^{87}Rb.

Transition Peak *F→F′*		**Initial State Energy (MHz)**	**Final State Energy (MHz)**	**Transition Energy (MHz)**
^{85}Rb	2→1	-1770.843	384230293.165	384232064.008
	2→(1,2)	-1770.843	384230307.851	384232078.694
	2→2	-1770.843	384230322.537	384232093.380
	2→(1,3)	-1770.843	384230339.552	384232110.395
	2→(2,3)	-1770.843	384230354.238	384232125.081
	2→3	-1770.843	384230385.938	384232156.781
	3→2	1264.888	384230322.537	384229057.649
	3→(2,3)	1264.888	384230354.238	384229089.350
	3→3	1264.888	384230385.938	384229121.050
	3→(2,4)	1264.888	384230414.558	384229149.670
	3→(3,4)	1264.888	384230446.258	384229181.370
	3→4	1264.888	384230506.578	384229241.690
^{87}Rb	1→0	-4271.676	384230128.395	384234454.071
	1→(0,1)	-4271.676	384230218.515	384234490.191
	1→1	-4271.676	384230254.635	384234526.311
	1→(0,2)	-4271.676	384230269.976	384234541.652
	1→(1,2)	-4271.676	384230333.096	384234604.772
	1→2	-4271.676	384230411.557	384234683.233
	2→1	2561.005	384230254.617	384227693.612
	2→(1,2)	2561.005	384230333.087	384227772.082
	2→2	2561.005	384230411.557	384227850.552
	2→(1,3)	2561.005	384230466.413	384227905.408
	2→(2,3)	2561.005	384230544.883	384227983.878
	2→3	2561.005	384230678.208	384228117.203

Table 7 The spacing in energy hyperfine levels with cross-over resonance of the D_2 line transition of ^{85}Rb and ^{87}Rb.

Transition Peak $F \rightarrow F'$		**Transition Energy (MHz)**	**Final State Energy (MHz)**	**Interval Ratio**
^{85}Rb	2→1	384232064.008		1:1:1:1:2
			14.686	
	2→(1,2)	384232078.694		
			14.686	
	2→2	384232093.380		
			17.015	
	2→(1,3)	384232110.395		
			14.686	
	2→(2,3)	384232125.081		
			31.700	
	2→3	384232156.781		
	3→2	384229057.649		1:1:1:1:2
			31.701	
	3→(2,3)	384229089.350		
			31.700	
	3→3	384229121.050		
			28.620	
	3→(2,4)	384229149.670		
			31.107	
	3→(3,4)	384229181.370		
			60.320	
	3→4	384229241.690		

Table 8 (Continued) The spacing in energy hyperfine levels with cross-over resonance of the D_2 line transition of ^{85}Rb and ^{87}Rb.

Transition Peak $F \rightarrow F'$		**Transition Energy (MHz)**	**Final State Energy (MHz)**	**Interval Ratio**
^{87}Rb	1→0	384234454.071	36.120	1:1:1:1:2
	1→(0,1)	384234490.191	36.120	
	1→1	384234526.311	42.341	
	1→(0,2)	384234568.652	36.120	
	1→(1,2)	384234604.772	78.461	
	1→2	384234683.233		
	2→1	384227693.612	78.470	2:2:1:2:3
	2→(1,2)	384227772.082	78.470	
	2→2	384227850.552	54.856	
	2→(1,3)	384227905.408	78.470	
	2→(2,3)	384227983.878	133.326	
	2→3	384228117.203		

2.8 Isotope Effect

In addition to the hyperfine interaction in Equation (14) there are several other effects that may have comparable magnitude [9], [23]. One of these is isotope effect or isotope shift, a small difference in transition energy between different isotopes of an element. The nuclear properties which give rise to isotope shift are the finite mass and the extended charge distribution of the nucleus, and also called mass effect and volume effect, respectively.

For one-electron atoms, the mass effect is taken into account by the introduction of the reduced mass of the electron and nucleus. For many-electron atoms, the finiteness of the nuclear mass induces an additional energy shift. By considering the kinetic energy operator in Schrödinger's equation

$$\mathbf{T} = \frac{\mathbf{p}_n^2}{2M} + \sum_i \frac{\mathbf{p}_i^2}{2m_0}, \tag{31}$$

where $\mathbf{p}_n$ and M are the momentum and mass of the nucleus, and $\mathbf{p}_i$ and m_0 are the momentum and mass of the ith electron. From conservation of momentum for a stationary atom

$$\mathbf{p}_n = -\sum_i \mathbf{p}_i \tag{32}$$

and Equation (31) may be rewritten as

$$\begin{aligned}\mathbf{T} &= \frac{\left(\sum_i \mathbf{p}_i\right)^2}{2M} + \frac{\sum_i \mathbf{p}_i^2}{2m_0} \\ &= \frac{\sum_i \mathbf{p}_i^2}{2M} + \frac{1}{M}\sum_{i>j}\mathbf{p}_i \cdot \mathbf{p}_j + \frac{\sum_i \mathbf{p}_i^2}{2m_0}.\end{aligned} \tag{33}$$

In the case of one-electron atoms, if at first we ignore the second term in Equation (33), the case of one-electron atoms, which contains the dot product of electron momenta, the remaining two terms can be combined with the reduced mass $m = \dfrac{m_0 M}{m_0 + M}$. Explicitly, an energy level $E(M)$ for an atom whose nucleus has a finite mass M is raised above the fictitious level $E(\infty)$ for an atom whose nucleus is infinitely heavy by a factor $\dfrac{M}{M + m_0}$

$$E(M) = E(\infty)\frac{M}{M + m_0}. \tag{34}$$

We choose $E(\infty)$ as a reference level and use the notation ΔE for $E(M) - E(\infty)$, so

$$\Delta E = -E(\infty)\frac{m_0}{M + m_0}. \tag{35}$$

For two isotopes whose nuclear masses, M and M', differ by δM we use the notation $\delta(\Delta E)$ for energy difference

$$\delta(\Delta E) \approx E(\infty)\frac{m_0 \delta M}{MM'}. \tag{36}$$

Finally, for the observed spectral line the wavenumber shift is

$$\delta\tilde{\nu} \approx \frac{m_0 \delta M}{MM'} \tilde{\nu}, \tag{37}$$

where the isotope of greater mass has the larger wavenumber. This phenomenon is known as the normal mass shift. In case of many-electron atoms, the cross term in Equation (33) leads to an additional isotope shift known as the specific mass shift. This term involves a correlation between the motions of a pair of electrons.

The difference in nuclear volume between isotopes can produce an isotope shift. Indeed, since the protons in the nucleus are distributed in a finite nuclear volume, the electrostatic potential inside the nucleus deviate from the $1/r$ law, and depends on the proton distribution within the nucleus. In order to obtain an estimate volume effect, let us consider a simple model of the nucleus, such that the nuclear charge is distributed in a uniform way within a sphere of radius

$$R = r_0 A^{1/3}, \tag{38}$$

where A is the mass number of the nucleus, and r_0 is a constant whose value is given approximately by $r_0 \approx 1.2 \times 10^{-15}$ m. In this model, the electrostatic potential $V(r)$ due to the nucleus is

$$V(r) = \begin{cases} \dfrac{Ze^3}{(4\pi\varepsilon_0)2R}\left(\dfrac{r^2}{R^2} - 3\right) & ; r \le R, \\ -\dfrac{Ze^3}{(4\pi\varepsilon_0)r} & ; r \ge R. \end{cases} \tag{39}$$

We will assume that the unperturbed Hamiltonian $\mathbf{H}_0$ is the hydrogen-like Hamiltonian and that the perturbation $\mathbf{H}'$ is the difference between the electrostatic potential $V(r)$ and the Coulombic interaction. Thus all other effects are neglected, the perturbation is given as

$$\mathbf{H}' = \begin{cases} \dfrac{Ze^3}{(4\pi\varepsilon_0)2R}\left(\dfrac{r^2}{R^2}+\dfrac{2R}{r}-3\right) & ; r \le R \\ 0 & ; r \ge R. \end{cases}, \tag{40}$$

The first order energy shift due to this perturbation is

$$\begin{aligned} \Delta E &= \langle \psi_{nlm} | \mathbf{H}' | \psi_{nlm} \rangle \\ &= \frac{Ze^3}{(4\pi\varepsilon_0)2R}\int_0^R |R_{nl}(r)|^2 \left(\frac{r^2}{R^2}+\frac{2R}{r}-3\right) r^2 dr. \end{aligned} \tag{41}$$

Inside the small region $r \le R$, we may write $R_{nl}(r) \simeq R_{nl}(0)$. Moreover, since $R_{nl}(0)$ vanishes except for s-states ($l = 0$), the energy shift becomes

$$\begin{aligned} \Delta E &\simeq \frac{Ze^2}{4\pi\varepsilon_0}\frac{R^2}{10}|R_{n0}(0)|^2 \\ &\simeq \frac{Ze^2}{4\pi\varepsilon_0}\frac{2\pi}{5}R^2 |\psi_{n00}(0)|^2 \\ &\simeq \frac{e^2}{4\pi\varepsilon_0}\frac{2}{5}R^2 \frac{Z^4}{a_\mu^3 n^3}, \end{aligned} \tag{42}$$

while $\Delta E \approx 0$ for states with $l \ne 0$. The difference of energy shift between two isotopes $\delta(\Delta E)$ whose charge distributions have radii R and $R + \delta R$, respectively, is

$$\begin{aligned} \delta(\Delta E) &\simeq \frac{Ze^2}{4\pi\varepsilon_0}\frac{4\pi}{5}R^2 |\psi_{n00}(0)|^2 \frac{\delta R}{R} \\ &\simeq \frac{Ze^2}{4\pi\varepsilon_0}\frac{4}{5}R^2 \frac{Z^4}{a_\mu^3 n^3}\frac{\delta R}{R}. \end{aligned} \tag{43}$$

We note that the isotope with the larger radius has the higher energy value, and $\delta\left(\Delta E\right)$ also increases when Z increases and n decreases. This implies that the most important volume effects occur for low-lying s-states (and on particular the ground state) of hydrogen-like atoms with larger Z.

In this case, rubidium, there are two natural abundant isotopes, the isotope effect could be applied to determine energy difference in the gross structure of ground state between both isotopes of rubidium as depicted in Figure 16. The ground state energy treated as hydrogen-like atom from the Bohr's model is -2.984×10^{-15} J .Then the isotope effects, the normal mass shift and the volume shift, are applied to the gross structure. The energy level of ^{85}Rb is chosen as reference level for determining the energy difference between both isotopes of rubidium.

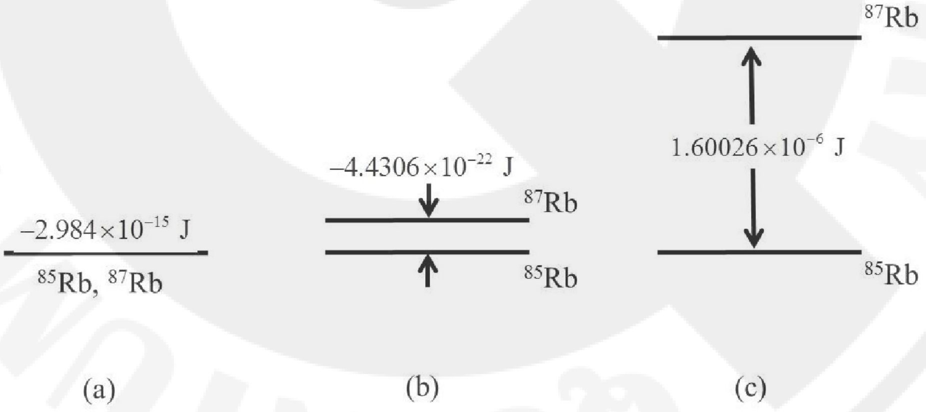

Figure 16 Ground state energy level of rubidium (a) Gross structure of the ground state (b) Normal mass shift and (c) Volume shift.

CHAPTER 3

EXPERIMENTAL SETUP

In this chapter, two experimental setups for the Doppler-free saturated absorption spectroscopy (DFSAS) for obtaining the hyperfine structure of rubidium were described. Firstly, the methods for tuning the ECDL that used as a light source in this research was provided. Next, the optical schematic arrangements for the DFSAS setups were introduced.

3.1 Tuning the ECDL

The source of driving energy in a typical setup of Doppler-free saturated absorption spectroscopy (DFSAS), illustrated in Figure 12, is our self-made external cavity diode laser (ECDL) (Figure 17). The laser design was adapted from a prototype made at the Atom Optics Group, University of Melbourne [6], where a mirror (Thorlabs, Part No. : BB05-E03-10) was added to a typical Littrow configuration [24-25]. This course of development provided a great advantage to optical alignment because continuous tilting the diffraction grating for frequency sweep will never change the direction of the zeroth order beam. Laser operation without mode-hoping is also necessary for low-noise spectrum profile. Such required stability was attainable via feedback controls of a steady current driver and temperature control circuit [2]. Simultaneously, the spectroscopy itself provide frequency feedback to a lock-in

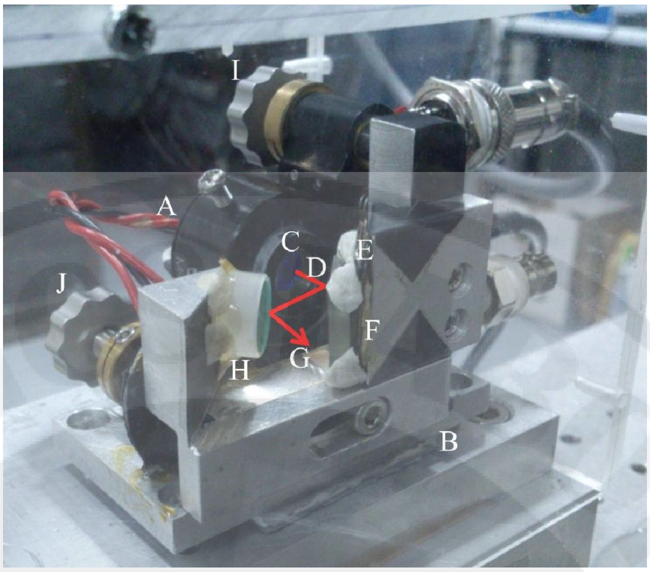

Figure 17 QAO lab's self-made external cavity diode laser. Current was fed to the diode through (A) and the thermoelectric cooler (B) controls the temperature of the diode (C). Multi-mode laser beam (D) gets diffracted by the grating (E) sitting in front of the piezo-stage (F) and the zeroth order beam (G) reflects at the dielectric mirror (H) [26].

circuitry that serves to fix the output laser beam at a particular frequency with respect to the atomic frame.

The self-made ECDL consists of a laser diode (Thorlabs, Part No. : L785P100) mounted in the collimation tube including aspheric collimating lens (Thorlabs, Part No. : LT110P-B) fixed to a mirror mount (Newport, Part No. : U100-P). The mirror mount was modified to L-shape for mounting the grating and mirror. The diffraction grating is gold coated holographic type, with 1,800 lines/mm on a 15x15x3.2 mm^3 substrate (Newport, Part No. : 33001FL02-330H). The grating was attached to the front face of the modified mirror mount, which provided vertical and horizontal grating adjustment. A piezoelectric transducer (PZT) disk under the grating was used to change the cavity length for fine frequency tuning. A temperature sensor (50 kΩ thermistor) and Peltier thermoelectric cooler (HB Corporation, Part No. : TEC1-12710) were used for temperature control.

Systematic series of continuous frequency tuning may be described as follows. The vertical and horizontal knobs (Newport, Part No. : AJS100-0.5K) (I and J in Figure 17) of the ECDL were first manually adjusted to send the first order beam back into the internal cavity of the laser diode. This optical feedback would increase stimulated emission rate at the feedback frequency. Since the tuning range must cover all the D_2 transitions, over feedback by using higher intensity of the first order beam that would result in less powerful output beam with wider tuning range (broader linewidth) was preferable.

The applied current was slightly adjusted under the threshold current of the diode, at which the diode started to flash with approximately 1 mW of power. The threshold current of the diode was approximately 0.8 V and obtained from the plot of emitted power versus applied voltage at the diode (Figure 18). The power meter (Thorlabs, Part No. : PM100USB) was used to monitor the zeroth order beam for continuous fine tuning. Both knobs were repeatedly adjusted to optimize the optical feedback to the diode and hence the laser power increased correspondingly to 3 – 4 mW. When the feedback frequency was optimized for the power output, our diode laser may give out 80 mW of stable beam at wavelength 780 nm. However, to compensate with the tunability that vary with the intensity of the first order beam, 5-10 mW is well enough for the DFSAS.

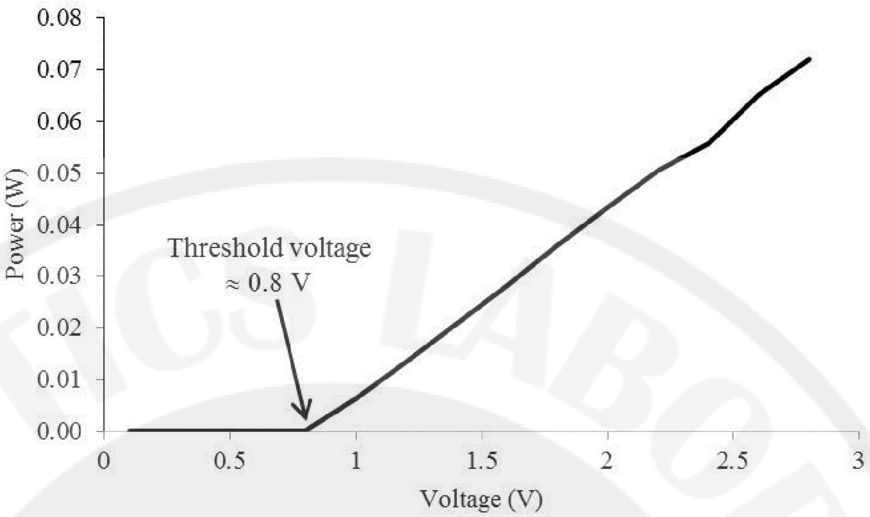

Figure 18 Plot of emitted power versus applied voltage at the diode. The threshold voltage is about 0.8 V, where at this point the diode started to flash.

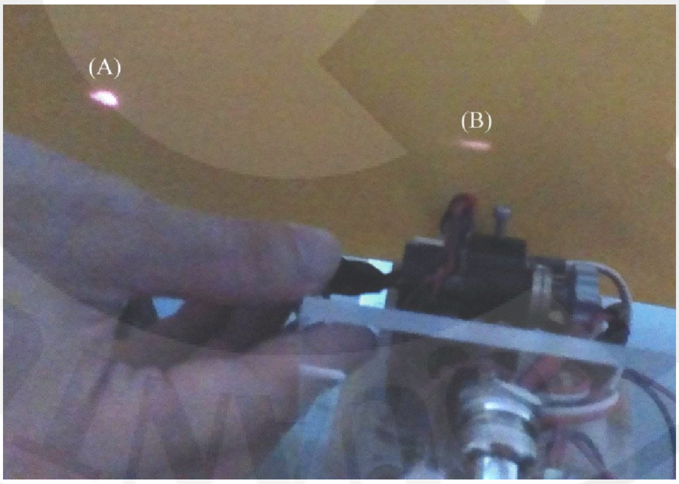

Figure 19 The zeroth order (A) and first order (B) laser beam on a paper sheet. The two beams were separated at the diffraction grating.

After that the spectrometer (Thorlabs, Part No. : CCS175) was used to observe the laser spectrum which directly reflects the tunability of the setup. When the ECDL was in a tunable range, the laser frequency could be later swept by tilting the diffraction grating (E in Figure 17). In the experiment, the emitted laser wavelength from the ECDL was tuned to 780 nm associated with a transition in the hyperfine structure from $5^2S_{1/2}$ to $5^2P_{3/2}$ of rubidium.

Furthermore, the laser is required to be in single mode operation without mode hopping. This prerequisites are attainable via feedback controls of a steady current driver and temperature control circuit as mentioned above. The laser stability would be affected by any source of vibration from environment, such as thermal disturbance, mechanical, and acoustical vibration. The thermal disturbance from air conditioning system would also impinge on temperature of the ECDL, and air flow from the air conditioner would cause the mechanical vibration disturbing the ECDL. To prevent these causes, temperature of the ECDL was controlled by the temperature control circuit, and covered by acrylic case [25]. Other sources of vibration especially vibration on an optical table would be taken care when running experiment to preserve the single mode operation of laser. The mode of laser was observed by using Fabry-Perot interferometer (Thorlabs, Part No. : SA210-5B) where the laser mode was monitored on an oscilloscope (Tektronix, Part No. : TDS2002B) as shown in Figure 20.

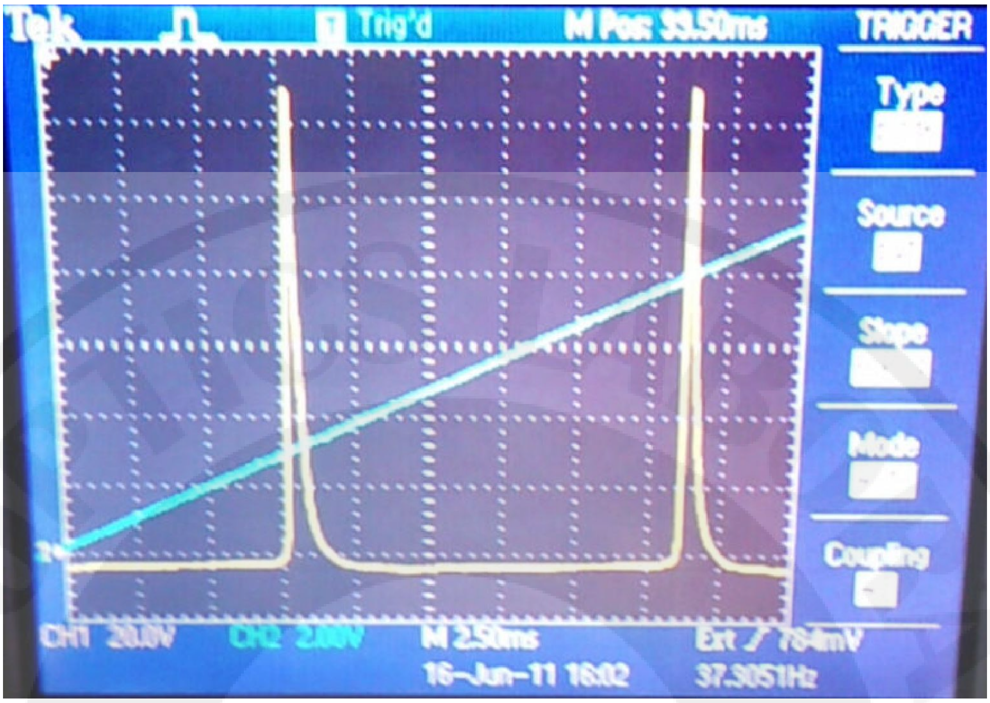

Figure 20 Single mode operation of the diode laser which was acquired from the Fabry-Perot interferometer.

3.2 Doppler-free Saturated Absorption Spectroscopy Setup

For a better insight of the true hyperfine structure of rubidium, two optical schemes associating with the propagation directions of the pump and probe beams were comparatively performed. The first configuration, small-angled crossing beams (less than 1 degree cross angle), consisted of typical optics as explained in Figure 12 and Figure 21 and the oscilloscope for monitoring the current-to-voltage signal. The second one, where both beams are fully antiparallel, requires additional one half-wave plate (Thorlabs, Part No. : WPH10M-780) and two polarizing beam splitters (Thorlabs, Part No. : PBS252) (Figure 22).

In the small-angled crossing beam configuration, the laser was split into three beams (Figure 13). Two low intensity beams (≈200μW) that reflected off the surfaces of an acrylic beam splitter were used as probe beams. The one that transmitted through the beam splitter having relatively much higher intensity (≈5mW) was used as a pump beam. The pump beam required laser intensity at least as 2 mW for rubidium atoms to pump most atoms to an excited state as mentioned in Chapter 2. Therefore, 5 mW of the pump beam is well enough for the DFSAS.

One of the probe beams that was sent through a vapor cell (Triad, Part No. : TT-RB-75-V-P) overlapped and counter propagated with the intense pump beam. The other passed through the atomic vapor cell without crossing the pump beam. Owing to the Doppler shift of the random thermal motion of atoms in the vapor cell, only the atoms with zero velocity with respect to both the pump and the probe beams interact with both beams at the same frequency. Since almost all of these atoms occupy the excited states due to the intense pump beam, the probe beam passed through the saturated part of the rubidium vapor as if it is transparent.

To acquire the absorption signal, each probe beam was sent into a photodiode. The current signal from the photodiodes contains dips on the Doppler broadening profile and the other without. The two photodiodes were wired such that the signal got subtracted and the Doppler broadening was eliminated. The intensity of the probe beams was converted into a voltage signal by the current-to-voltage amplifier circuit [2] and the spectra were displayed on the oscilloscope.

The other type of the DFSAS exploits two polarization beams splitters to allow zero cross angle between the pump and the probe beam. The ease of theoretical analysis is achievable at the expense of costly optical parts. Not without a half-wave plate, may the intensities of split beams be appropriately differentiated and the saturated dips be clearly visible. Though only one rubidium vapor cell would well do the job, two of them were used to earn more space for optical and electrical accessibilities. At the end, signal from the two probe beams were similarly subtracted and the Doppler broadening on the hyperfine structure absorption profile was suppressed.

For both schemes, to obtain the full hyperfine absorption spectra over all the D_2 lines of ^{85}Rb and ^{87}Rb, the frequency of the laser was linearly swept by varying the grazing angle of the grating via selectively injected current into the piezo-stage attached behind (F in Figure 17). The data acquisition can be performed by either directly taking pictures from the oscilloscope or exporting the excel file from a competent oscilloscope.

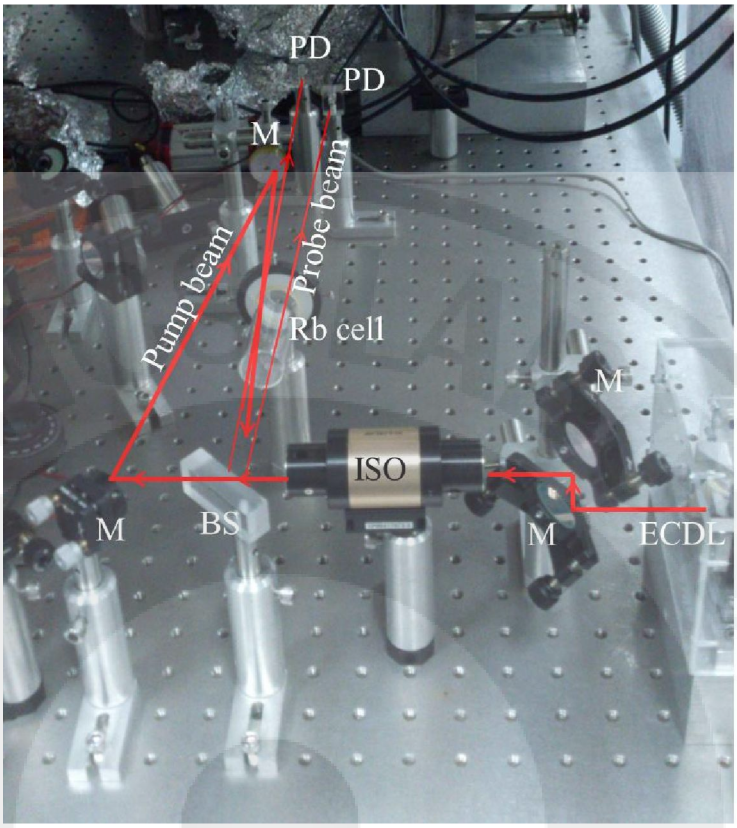

Figure 21 DFSAS setup with a small cross angle between pump and probe beams. All abbreviations are defined as following which also apply to figure 22: optical isolator (ISO) (Thorlabs, Part No. : IO-3-780-HP), acrylic beam splitter (BS), polarizing beam splitter (PBS), dielectric mirror (M) (Thorlabs, Part No. : BB05-E03), photodiode (PD) (Osram, Part No. SFH 213), and half-wave plate (λ/2) (Thorlabs, Part No. : WPH10M-780).

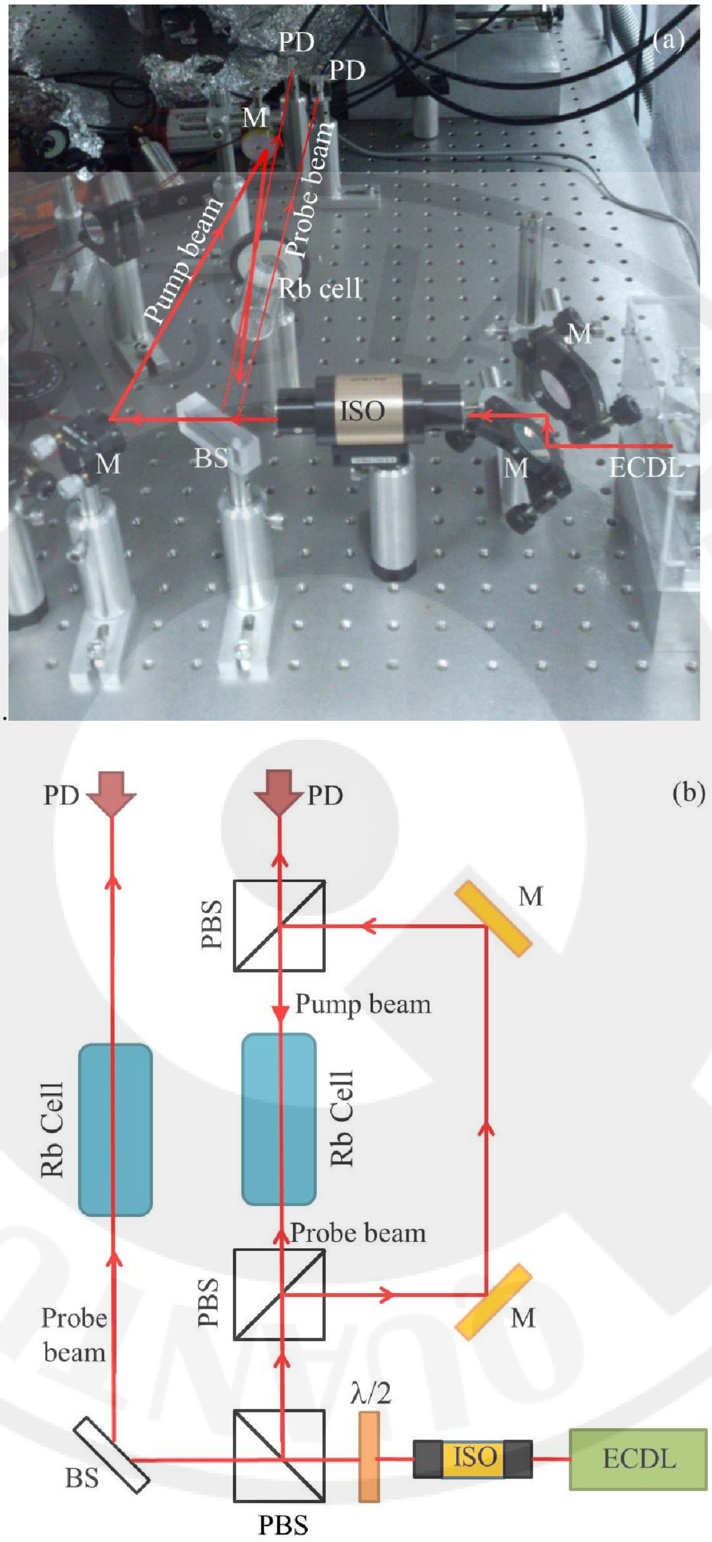

Figure 22 (a) DFSAS setup with zero cross angle between pump and probe beams (b) Schematic setup diagram. See the abbreviations in Figure 13.

CHAPTER 4

RESULTS AND DISCUSSIONS

In this chapter, results of this work, absorption spectra for the D_2 line of ^{85}Rb and ^{87}Rb that reflected the hyperfine structure were presented. The linewidth and interval ratio of obtained absorption profiles were extracted and compared with the theoretical calculation for confirming that the spectra represented the hyperfine structure of rubidium.

4.1 Doppler-free Saturated Absorption Spectra Results

The results of the two DFSAS experimental setups that were mentioned in the previous chapter (Figure 21 and Figure 22) are provided in this section. The comparison of the results between the two setups is given. Before we compare these results, the general descriptions of the DFSAS profiles are as follows. First of all, when there was only one probe beam passing through a rubidium vapor cell to a photodiode, an observed absorption spectrum showed the Doppler effect of atom-light interaction which is called Doppler broadening (Figure 23). This is the effect that the atoms in various velocity groups absorb light at different frequencies. The absorption profile with four fine structure lines was exposed. Secondly, the pump beam was applied in counter propagating direction of the other probe beam that also went across the vapor cell to a photodiode. The Doppler profile was affected by the counter propagating beams regarding to the following argument. The zero-velocity group of atoms interacted with both beams and almost all of atoms in the ground state were optically pumped to an excited state. The interaction of both laser beams caused the Doppler dips (Figure 24) near the center of the fine structure absorption peaks. These are the dips corresponding to the hyperfine structures. Finally, the intensities of the two probe lasers from the two photodiodes were converted into voltage signals. They were subtracted from each other to acquire the DFSAS spectrum (Figure 25).

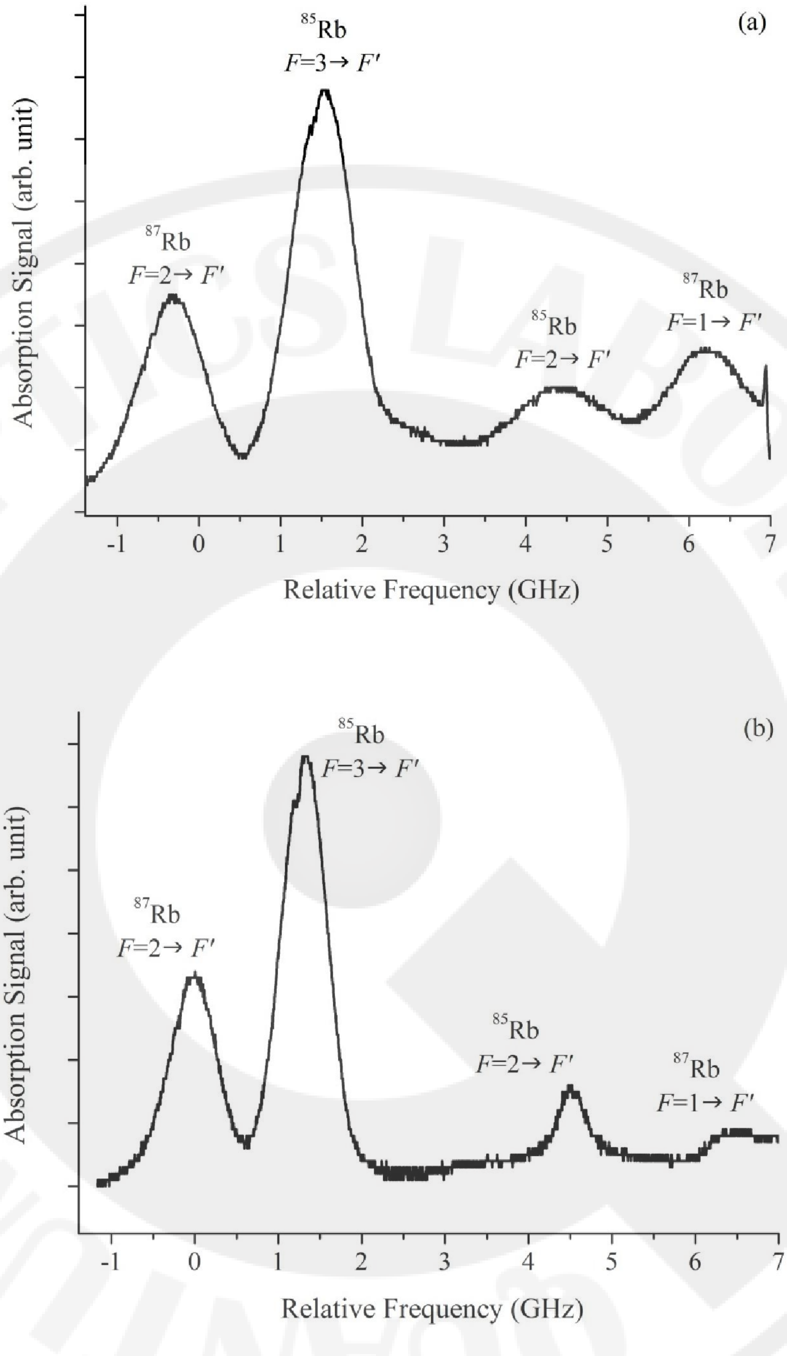

Figure 23 The Doppler broadening absorption spectra for the D_2 line transition of ^{85}Rb and ^{87}Rb. The labels with letter (a) and (b) refer to the small cross angle scheme and to zero cross angle scheme, respectively. The spectral profiles were acquired from an oscilloscope and plotted with OriginPro 8 and Microsoft Excel 2010.

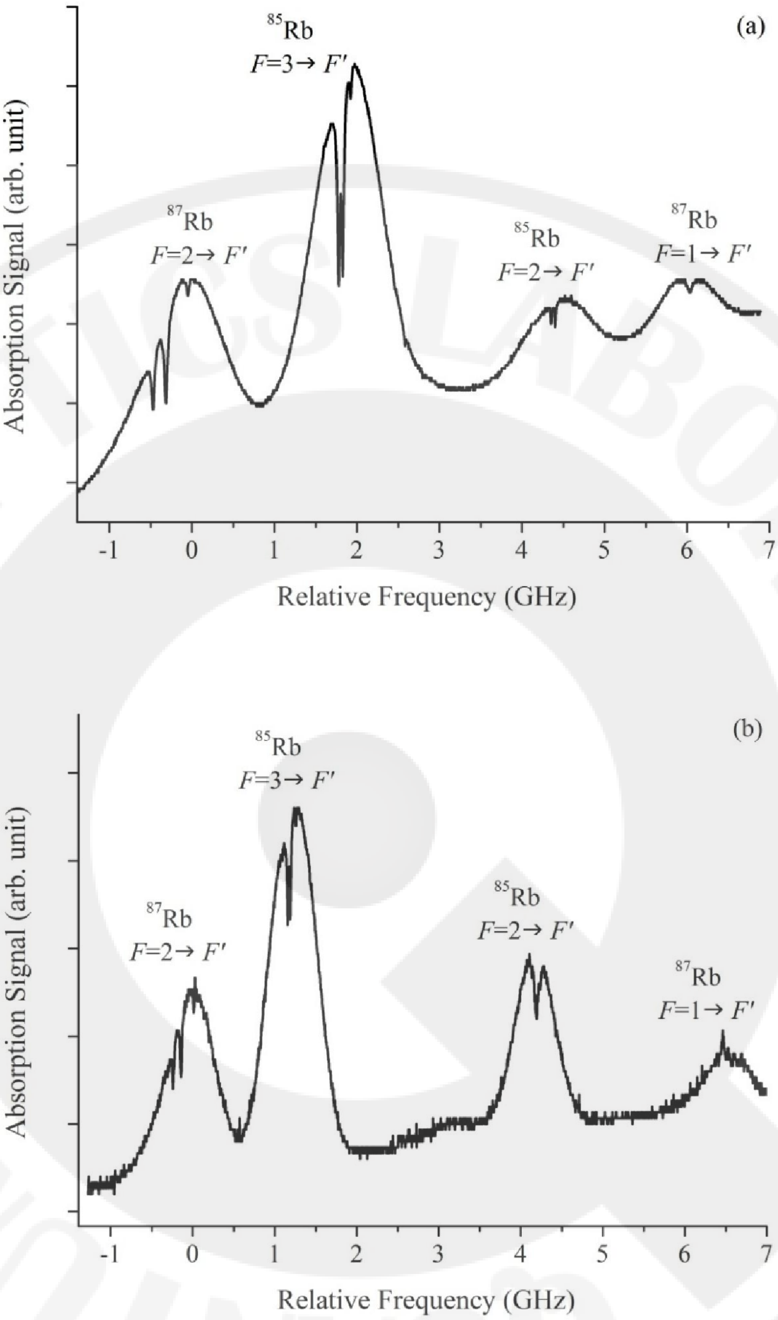

Figure 24 The absorption dips on the Doppler broadening profile of the D_2 line transition of ^{85}Rb and ^{87}Rb. The labels with letter (a) and (b) refer to the small cross angle scheme and to zero cross angle scheme, respectively. The spectral profiles were acquired from an oscilloscope and plotted with OriginPro 8 and Microsoft Excel 2010.

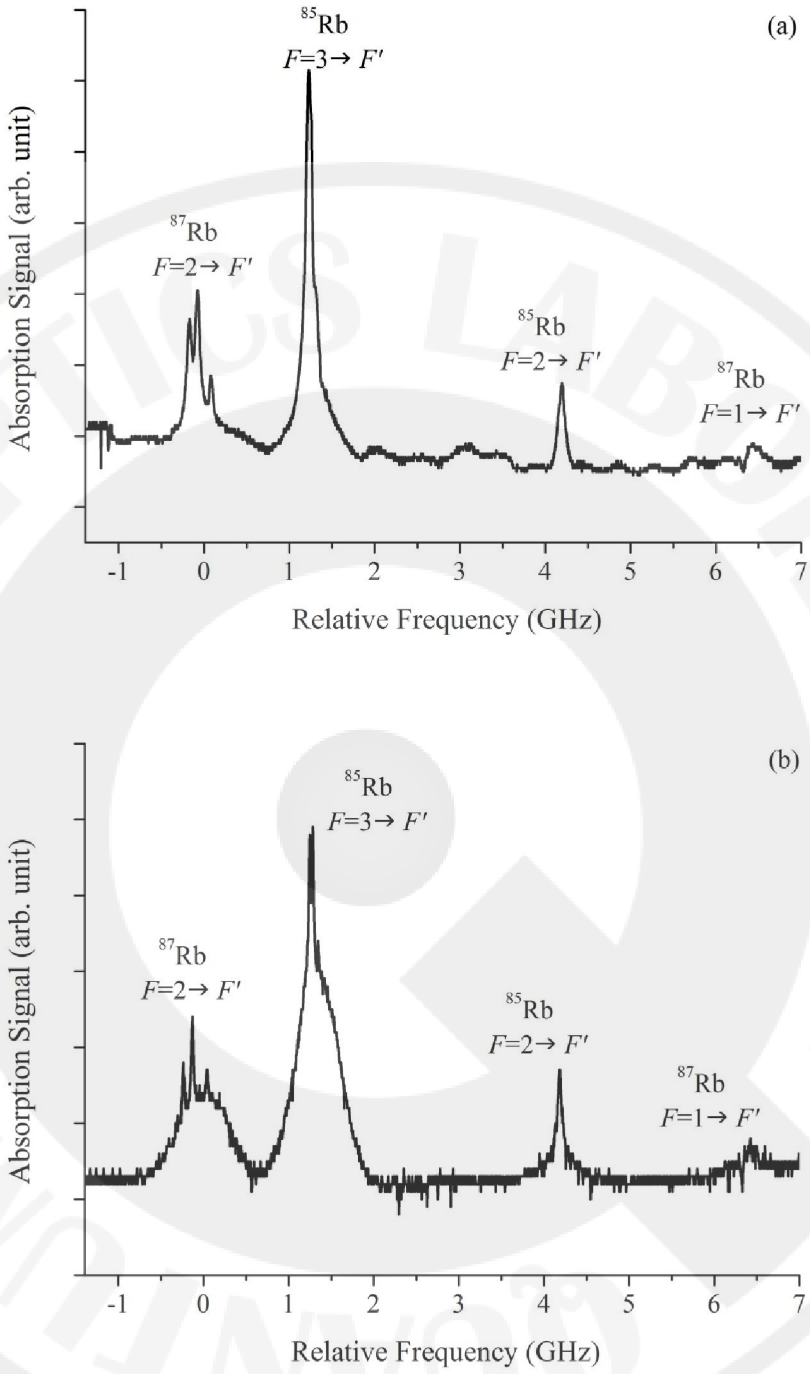

Figure 25 The DFSAS profile of the D_2 line transition of ^{85}Rb and ^{87}Rb. The labels with letter (a) and (b) refer to the small cross angle scheme and to zero cross angle scheme, respectively. The spectral profiles were acquired from an oscilloscope and plotted with OriginPro 8 and Microsoft Excel 2010.

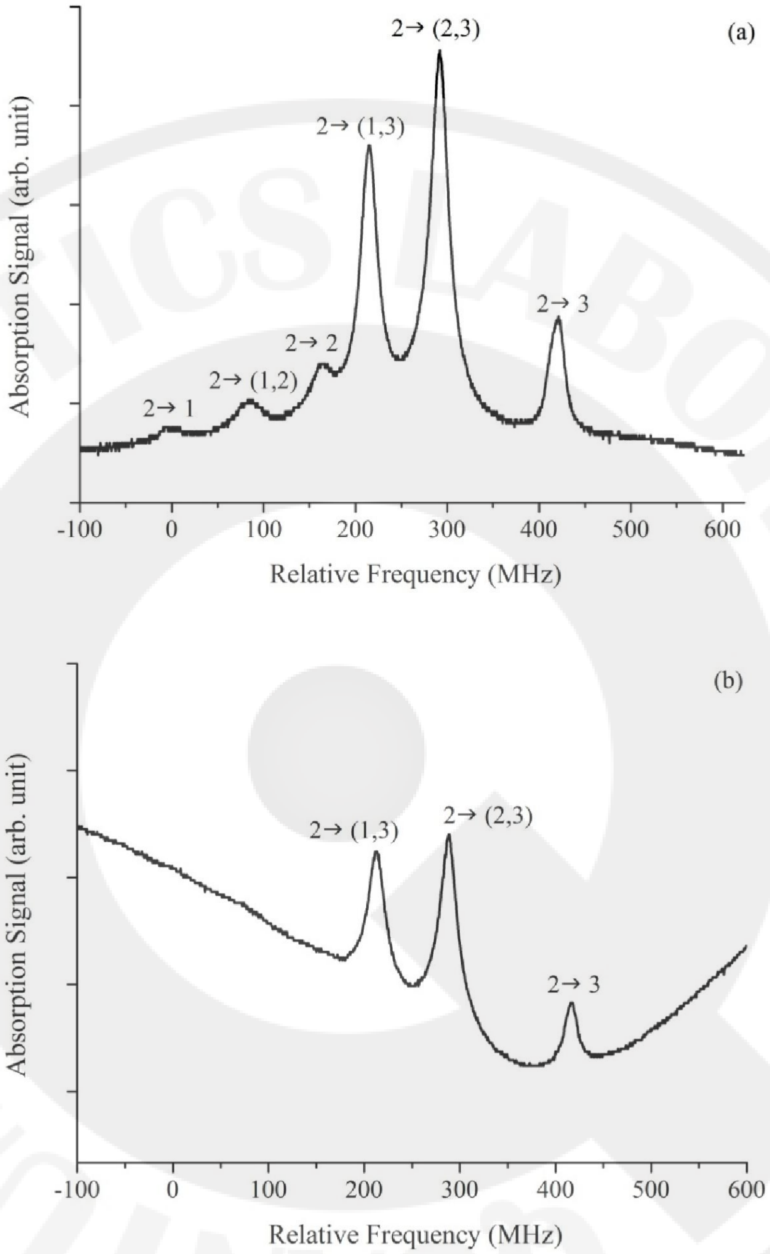

Figure 26 The DFSAS spectrum for *F*=2 to *F′* of ^{87}Rb. The bracketed numbers refer to cross-over transitions. The labels with letter (a) and (b) refer to the small cross angle scheme and to zero cross angle scheme, respectively. The spectral profiles were acquired from an oscilloscope and plotted with OriginPro 8 and Microsoft Excel 2010.

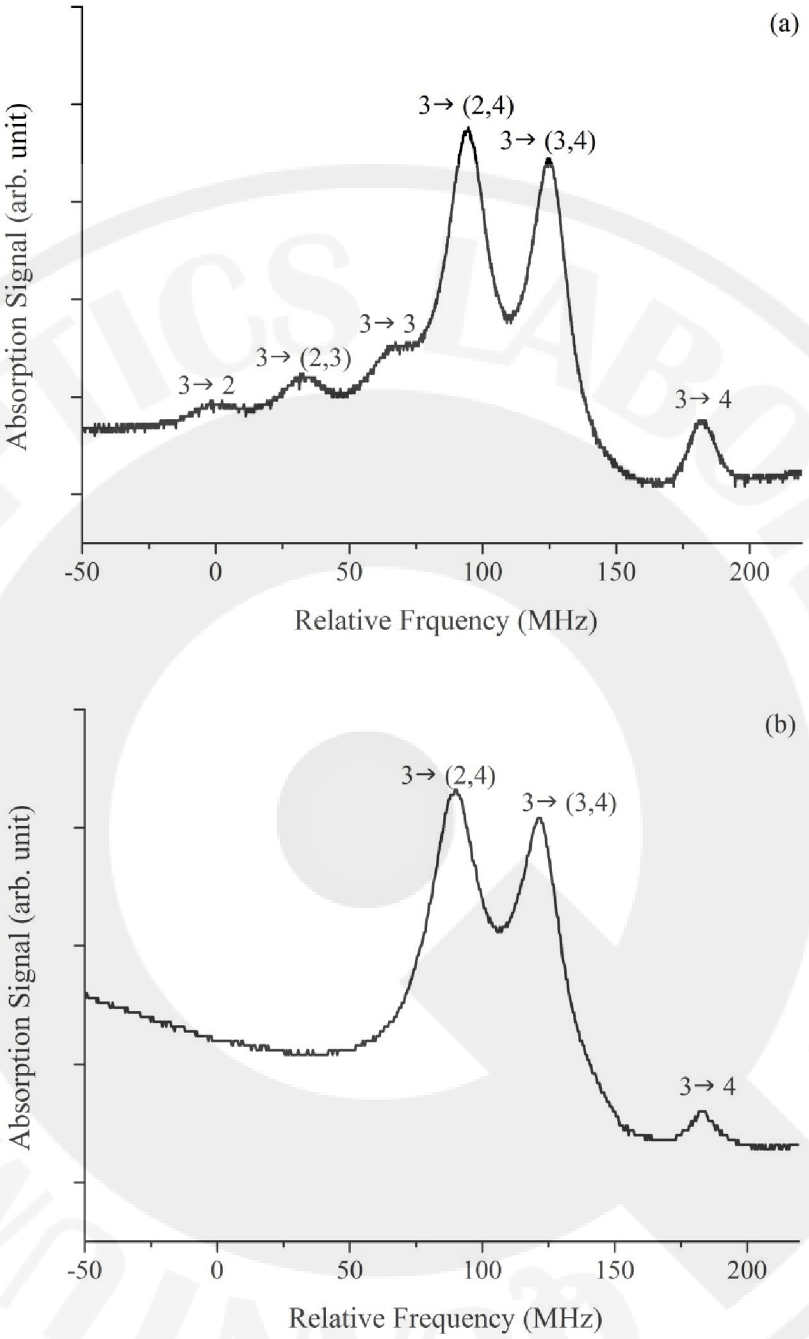

Figure 27 The DFSAS spectrum for *F*=3 to *F′* of ^{85}Rb. The bracketed numbers refer to cross-over transitions. The labels with letter (a) and (b) refer to the small cross angle scheme and to zero cross angle scheme, respectively. The spectral profiles were acquired from an oscilloscope and plotted with OriginPro 8 and Microsoft Excel 2010.

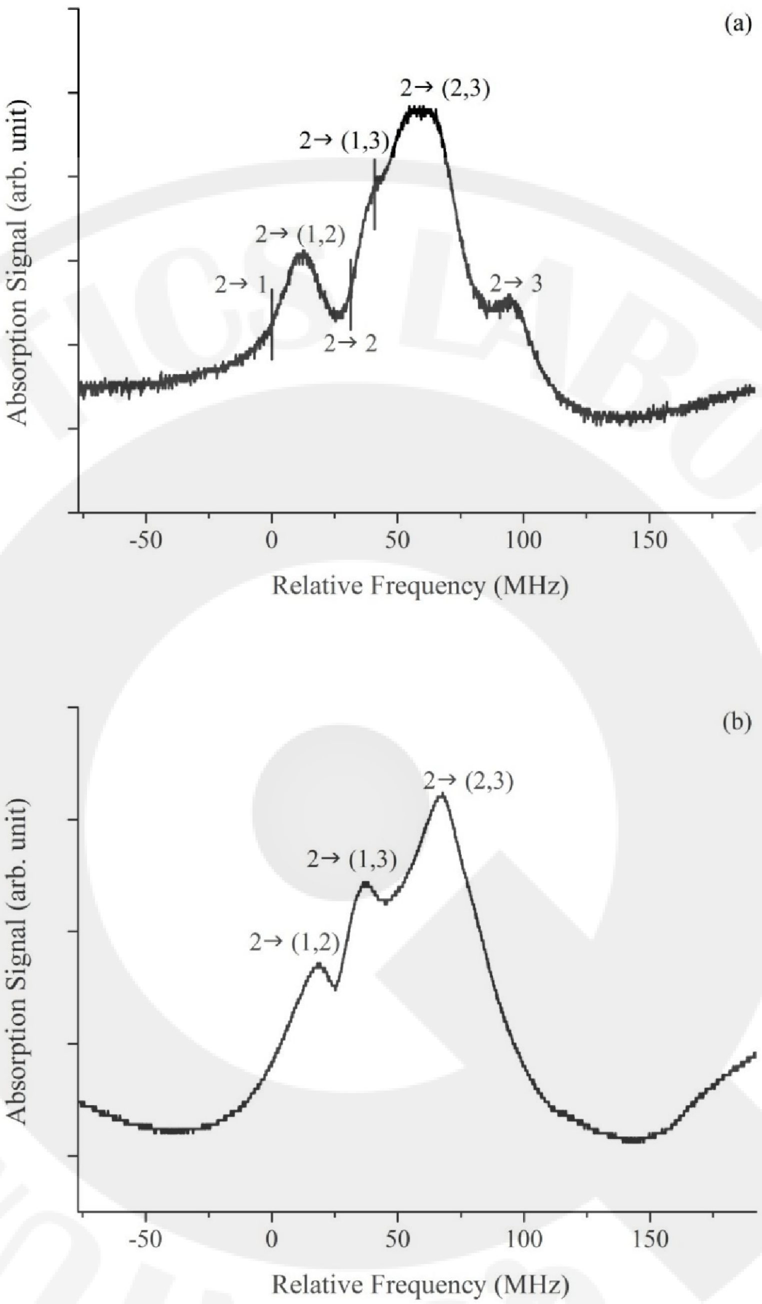

Figure 28 The DFSAS spectrum for F=2 to F' of ^{85}Rb. The bracketed numbers refer to cross-over transition. The labels with letter (a) and (b) refer to the small cross angle scheme and to zero cross angle scheme, respectively. The spectral profiles were acquired from an oscilloscope and plotted with OriginPro 8 and Microsoft Excel 2010.

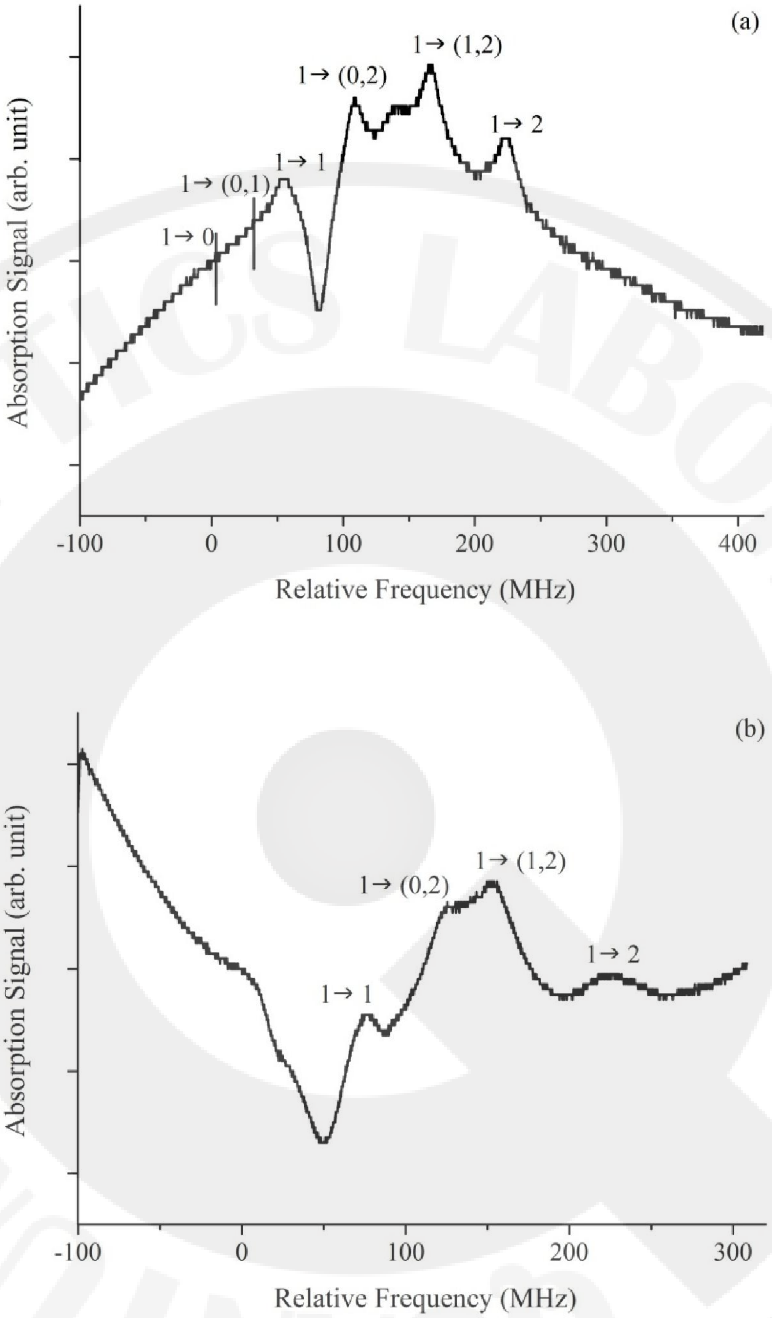

Figure 29 The DFSAS spectrum for *F*=1 to *F′* of ^{87}Rb. The bracketed numbers refer to cross-over transitions. The labels with letter (a) and (b) refer to the small cross angle scheme and to zero cross angle scheme, respectively. The spectral profiles were acquired from an oscilloscope and plotted with OriginPro 8 and Microsoft Excel 2010.

4.2 Discussions

4.2.1 The DFSAS Spectra

The DFSAS experiment was performed at room temperature 21ºC. As previously mentioned in Chapter 2, the linewidth depends on the velocity distribution of the gas. By using the ideal gas equation and kinetic theory of gas, the velocity distribution of gas at room temperature was related with the linewidth of the DFSAS spectrum. The average velocity of the gas in the vapor cell at room temperature, Equation (23), was 292.89 m/s. Therefore, the Doppler linewidth of both rubidium isotopes were calculated as 511.93 MHz for ^{85}Rb and 515.41 MHz for ^{87}Rb by Equation (28).

The acquired spectra of the two schematic setups from the oscilloscope were plotted with relative transition frequencies. The relative transition frequencies of the D_2 line of ^{85}Rb and ^{87}Rb are obtained from Figure 5. By fitting pixel position of absorption peaks with the transition frequencies, linear equation for converting the pixel position to frequency was determined. For example, there were four peaks of the fine structure transition in Figure 23(a), and their pixel positions with relative transition frequencies were tabulated in Table 8.

Table 8 The pixel position and relative transition frequency of the fine structure peaks in Figure 23(a).

Peak	Pixel Position	Relative Frequency (GHz)
^{87}Rb $F = 2 \rightarrow F'$	264.214	0.000
^{85}Rb $F = 3 \rightarrow F'$	570.443	1.126
^{85}Rb $F = 2 \rightarrow F'$	1322.952	4.042
^{87}Rb $F = 1 \rightarrow F'$	1762.960	6.563

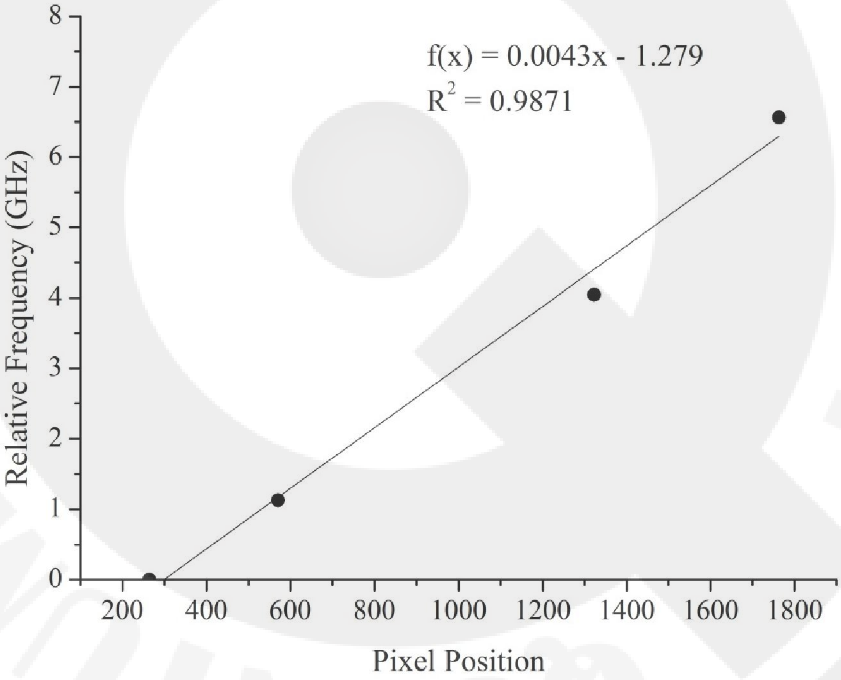

Figure 30 Calibration plot for the fine structure peaks (Figure 23(a)). The relative frequencies of the peaks are plotted against their pixel position as given by the oscilloscope. The equation for the linear fit is shown.

As there was only the probe laser beam passing through the vapor cell to the photodiode, the Doppler broadening occurred on the absorption profile due to the atom-light interaction. The linewidth of the profile from the two types of experimental setup, small cross angle and zero cross angle, was analyzed by OriginPro8 as well as shown in Table 9. The observed linewidths from thetransition ^{87}Rb $F = 2 \rightarrow F'$, ^{85}Rb $F = 3 \rightarrow F'$, and ^{85}Rb $F = 2 \rightarrow F'$ are in good agreement with the theoretical calculation in order of 500 MHz.

Table 9 The observed Doppler linewidth of the D_2 line transition of both schematic setups of DFSAS (Figure 23).

Fine Structure Peak	**Linewidth (MHz)**	
	Small Cross Angle	**Zero Cross Angle**
^{87}Rb $F = 2 \rightarrow F'$	562.85	553.83
^{85}Rb $F = 3 \rightarrow F'$	515.95	533.40
^{85}Rb $F = 2 \rightarrow F'$	543.77	507.16
^{87}Rb $F = 1 \rightarrow F'$	985.95	965.44

In presence of the pump beam propagating in the opposite direction with the probe beam, the Doppler broadening linewidth would be narrowed close to the natural linewidth, about 40 MHz as shown in Chapter 2. There are other broadening mechanisms; some cannot be eliminated such as the pressure and intensity broadening because they are not related to velocity distribution of the atoms. The spectral linewidth decreased due to the suppression of the Doppler effect. At this point, the hyperfine structure of ^{85}Rb and ^{87}Rb could be monitored by zooming at the oscilloscope onto the Doppler dips on the subtracted profile. In the situation that atoms interact with a radiation, the spontaneous emission lifetime of the excited state and Heisenberg uncertainty principle suggested that the hyperfine spectra have a Lorentzian profile. The observed hyperfine spectral width is shown in Table 10.

Table 10 The hyperfine structure width of 85Rb and 87Rb of the two experimental setup types were measured for the two experimental schemes (Figure 26-29).

Transition Peak ($F \rightarrow F'$)		Linewidth (MHz)	
		Small Cross Angle	**Zero Cross Angle**
Figure 26 (^{87}Rb)	$2 \rightarrow 1$	22.27	N/A
	$2 \rightarrow (1,2)$	28.91	N/A
	$2 \rightarrow 2$	25.45	N/A
	$2 \rightarrow (1,3)$	42.80	47.82
	$2 \rightarrow (2,3)$	49.92	16.35
	$2 \rightarrow 3$	35.22	26.88
Figure 27 (^{85}Rb)	$3 \rightarrow 2$	779.11	N/A
	$3 \rightarrow (2,3)$	16.02	N/A
	$3 \rightarrow 3$	20.18	N/A
	$3 \rightarrow (2,4)$	30.43	638.95
	$3 \rightarrow (3,4)$	26.47	20.52
	$3 \rightarrow 4$	49.69	34.29
Figure 28 (^{85}Rb)	$2 \rightarrow 1$	2.04	N/A
	$2 \rightarrow (1,2)$	22.39	26.53
	$2 \rightarrow 2$	3.23	N/A
	$2 \rightarrow (1,3)$	25.98	22.23
	$2 \rightarrow (2,3)$	23.62	11.89
	$2 \rightarrow 3$	10.17	N/A
Figure 29 (^{87}Rb)	$1 \rightarrow 0$	211.19	N/A
	$1 \rightarrow (0,1)$	69.88	N/A
	$1 \rightarrow 1$	21.42	401.10
	$1 \rightarrow (0,2)$	20.58	25.97
	$1 \rightarrow (1,2)$	37.71	19.63
	$1 \rightarrow 2$	40.60	76.14

The acquired hyperfine spectra from oscilloscope of the two experimental setup schemes as shown in Figure 26 – Figure 29 were plotted within the same relative frequency scale for each transition. The absorption peaks are determined by the relative frequencies from Figure 5. The transitions in hyperfine levels satisfy the selection rule, Equation (21), and hence, there are three absorption peaks for each pair of transitions from ground state to first excited states. Though, other three peaks (cross-over resonance peaks) also appeared on the profile owing to the effect of sharing a common ground state in the transition as mentioned in Chapter 2. According to the cross-over resonance peaks occurring in the hyperfine level transition, its spectral width is similar to the hyperfine width.

Refer to the hyperfine linewidth which was assayed by OriginPro8 in Table 10, some of them in the fully counter-propagating beams setup are not applicable labeling with N/A because the peaks can be not determined on the profile. The vagueness in the profile that obtained from the zero cross angle setup came from the working condition of the ECDL, which was not in a pure single mode, and signal subtraction of the two photodiodes that was not well subtracted. According to the single mode running of the ECDL, there are some factors related to the working condition such as the stability of applied current and the temperature of the ECDL, and the vibration from environment. The fully counter-propagating beam experimental setup while has been conducting the temperature was not stable. Any source of vibration such as slamming the door, walking, or loudly talking affect the single mode operation as well. Moreover, laser intensity of the pump and the probe beam in the zero cross angle setup were slightly different, some absorption peak is obscured from the profile. To resolve the problem of the laser intensity, another half-wave plate should be placed between the beam splitter in the setup (Figure 22) for adjusting the laser intensity of the pump beam.

Additionally, the cross-over resonance peaks on the absorption profiles dominated over the main hyperfine transition peaks as figured in the hyperfine spectral results in Figure 26 – Figure 29. As mentioned in Chapter 2, the cross-over resonance produced extra peaks on the major transition because some moving atoms in the laser saw a frequency shift to the exact resonance frequency from the Doppler effect. The laser reached the resonance frequency of two excited hyperfine states sharing the one common hyperfine ground state. The ground state population of the moving atoms in the Maxwell-Boltzmann velocity distribution depleted into the excited state much more than the number of the stationary atoms, relative to the propagating direction of the laser. The atoms were excited at the exact resonance frequency as shown in Figure 31. Therefore, the cross-over resonance peaks were higher than the major absorption peaks on the hyperfine spectra.

4.2.2 The Landè Interval Rule

According to Equation (16), the energy hyperfine structure is proportional to the total angular momentum quantum number F which is relative to the nuclear spin angular momentum quantum number I and to the electron total angular momentum quantum number J. The separation of adjacent multiplet hyperfine levels is corresponding to F of the higher level. The energy spacing ratio or interval ratio of the first excited state hyperfine structure including the cross-over resonance of ^{85}Rb and ^{87}Rb, therefore, can be understood by using the Landè interval rule (an example is

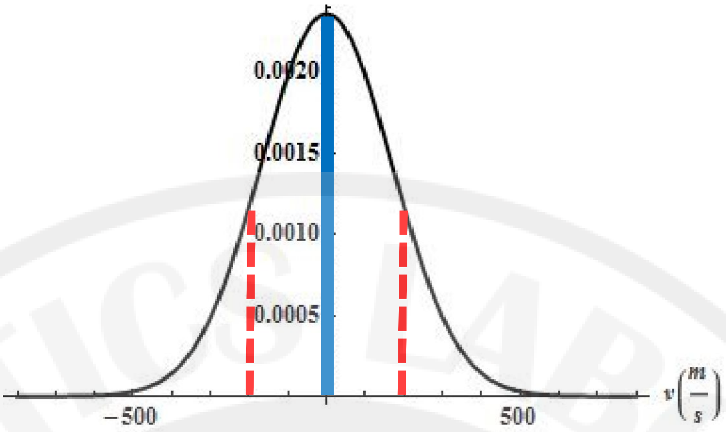

Figure 31 The Maxwell-Boltzmann velocity distribution of the atoms in the ground state. The dashed line represents the population of atoms in upper state from the atoms moving along the laser propagation. The bold line represents the population of the zero-velocity atoms that have been excited into the upper level at the exact resonance frequency.

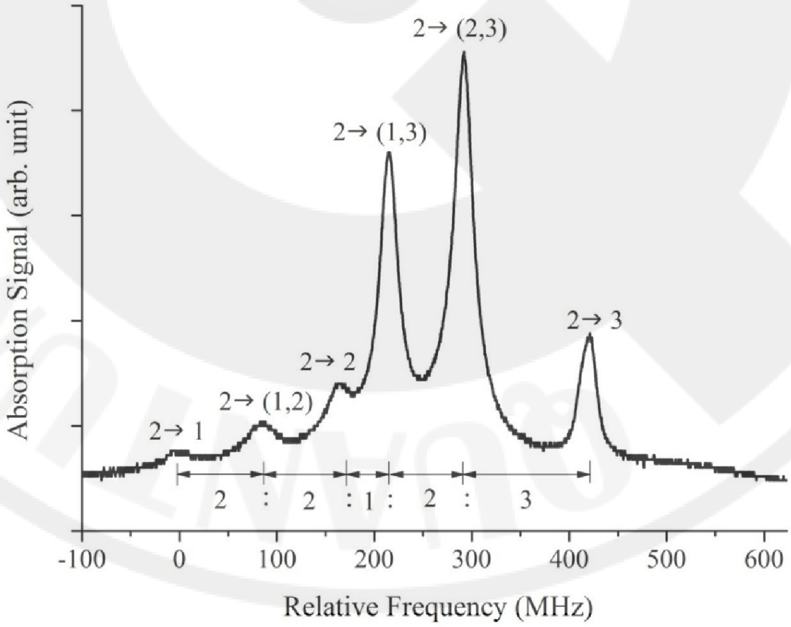

Figure 32 The Landè interval rule for the absorption profile of the transition *F*=2 to *F′* of ^{87}Rb obtaining from the small cross angle setup.

shown in Figure 32). The transition frequency of the hyperfine peaks was extracted by assistance of OriginPro8, and the value of spacing in energy (frequency) for the hyperfine levels transition of the two experimental setups is also demonstrated in Table 11. The ratio of frequency spacing on the observed hyperfine spectral and the theoretical calculation value of Table 7 was compared in Table 12.

Table 11 The spacing in frequency for ^{85}Rb and ^{87}Rb hyperfine spectra (Figure 26-29) obtained from the small cross angle and zero cross angle setup. All spacing in frequency are shown against the theoretical calculation.

Transition Peak	**(*F*→*F'*)**	**Frequency (MHz)**		**Spacing (MHz)**		
		Small Cross Angle	**Zero Cross Angle**	**Small Cross Angle**	**Zero Cross Angle**	**Theoretical Calculation**
Figure 26 (^{87}Rb)	2 → 1	-1.070	N/A	85.617	N/A	78.470
	2 → (1,2)	84.547	N/A	80.475	N/A	78.470
	2 → 2	165.022	N/A	49.919	N/A	54.856
	2 → (1,3)	214.941	212.541	75.937	74.917	78.470
	2 → (2,3)	290.878	287.458	130.395	130.811	133.326
	2 → 3	421.273	418.269			
Figure 27 (^{85}Rb)	3 → 2	0.021	N/A	32.447	N/A	31.701
	3 → (2,3)	32.468	N/A	33.010	N/A	31.700
	3 → 3	65.478	N/A	28.841	N/A	28.620
	3 → (2,4)	94.319	89.475	30.644	32.446	31.700
	3 → (3,4)	124.963	121.921	57.007	61.288	60.320
	3 → 4	181.970	183.209			

Table 11 (Continued) The spacing in frequency for the 85Rb and 87Rb hyperfine spectra (Figure 26-29) obtained from the small cross angle and zero cross angle setup. All spacing in frequency are shown against the theoretical calculation.

Transition Peak ($F \rightarrow F'$)		Frequency (MHz)		Spacing (MHz)		
		Small Cross Angle	Zero Cross Angle	Small Cross Angle	Zero Cross Angle	Theoretical Calculation
Figure 28 (^{85}Rb)	2 → 1	0.035	N/A	11.355	N/A	14.686
	2 → (1,2)	11.390	18.023	19.225	N/A	14.686
	2 → 2	30.615	N/A	9.557	N/A	17.015
	2 → (1,3)	40.172	37.249	21.024	29.927	14.686
	2 → (2,3)	61.196	67.176	32.179	N/A	31.700
	2 → 3	95.375	N/A			
Figure 29 (^{87}Rb)	1 → 0	-1.946	N/A	31.553	N/A	36.120
	1 → (0,1)	29.607	N/A	24.555	N/A	36.120
	1 → 1	54.162	71.410	54.812	51.475	42.341
	1 → (0,2)	108.974	122.885	57.224	30.920	36.120
	1 → (1,2)	166.198	153.805	57.443	68.340	78.461
	1 → 2	223.641	222.145			

Table 12 The observed hyperfine structure spacing ratio and its theoretical values.

Transition Peak ($F \rightarrow F'$)		**Hyperfine Structure Spacing Ratio**		
		Small Cross Angle	**Zero Cross Angle**	**Theoretical Calculation**
Figure 26 (^{87}Rb)	2 → 1	2	N/A	2
	2 → (1,2)	2	N/A	2
	2 → 2	1	N/A	1
	2 → (1,3)	2	1	2
	2 → (2,3)	3	2	3
	2 → 3			
Figure 27 (^{85}Rb)	3 → 2	1	N/A	1
	3 → (2,3)	1	N/A	1
	3 → (2,4)	1	N/A	1
	3 → (3,4)	1	1	1
	3 → 4	2	2	2
Figure 28 (^{85}Rb)	2 → 1	1	N/A	1
	2 → (1,2)	2	N/A	1
	2 → 2	1	N/A	1
	2 → (1,3)	2	-	1
	2 → (2,3)	3	N/A	2
	2 → 3			
Figure 29 (^{87}Rb)	1 → 0	1	N/A	1
	1 → (0,1)	1	N/A	1
	1 → 1	2	2	1
	1 → (1,2)	2	1	1
	2 → (2,3)	2	2	2
	1 → 2			

The values of the frequency spacing for the hyperfine level transition of ^{85}Rb and ^{87}Rb, which were taken from the both experimental schemes as shown in Table 11, correspond to the calculated value from the theory that obtained from the energy level diagram, Figure 5. Some of the interval ratios, however, are not in agreement with the theoretical calculation especially the profile of the transition F=2 to F' of ^{85}Rb (Figure 28) and F=1 to F' of ^{87}Rb (Figure 29) because absorption peaks is not well resolved into the profile. Thus an indication of the absorption peaks cannot be identified accurately. Nevertheless, the dominant peaks that can be observed and specified their positions on the profile give the values of the frequency separation that agree with the theoretical values as shown in Table 12. The not perfect resolvability of the spectrum, particularly in Figure 28 and Figure 29 including the results of the fully counter propagating beam experiment, can be traced back to several factors such as the stability of the ECDL, the broadening of the laser intensity, and the electronic noises from circuitries. Another remark of the Landè interval rule is shown in Table 4. The result of the interval ratio for the hyperfine levels of ^{85}Rb is 4:3:2 with the calculation of energy by using Equation (14) and Equation (16), but the observed values of its hyperfine levels give the ratio as 4:2:1 illustrated in the bracket. This disagreement in the ratio of ^{85}Rb levels can be understood in the analysis of the isotope effect. The consequent on the same coarse atomic structures giving that they are distinguished from one another by their mass as mentioned in Chapter 2.

CHAPTER 5

CONCLUSIONS AND FUTURE PLANS

5.1 Conclusions

In the experiment, the spectroscopic technique (DFSAS), which was used to suppress the broadening on the absorption spectrum, was set up for investigating the hyperfine structure of ^{85}Rb and ^{87}Rb in two schemes using the self-made external cavity diode laser (ECDL). The ECDL was also stabilized and maintained under the working condition: single mode operation without laser mode hopping. The stable ECDL was tuned to 780 nm to cover the D_2 line transition of ^{85}Rb and ^{87}Rb. The absorption profiles were obtained from the two optical setups associating with the propagation directions of the pump and probe beams, i.e., small cross angle and zero cross angle.

In order to monitor the hyperfine structure, the Doppler broadening was eliminated from the absorption profile by the advantage of the intense pump beam. The narrow linewidth spectrum was obtained by subtracting the two probing signal from two photodiodes and four absorption profiles for the hyperfine level transitions in both DFSAS setup schemes were acquired. The four spectra represent the hyperfine level changing, two from ^{85}Rb: $F = 2 \rightarrow F'$, $F = 3 \rightarrow F'$, and two from ^{87}Rb: $F = 1 \rightarrow F'$, $F = 2 \rightarrow F'$. The transitions satisfy the selection rule, and the three absorption peaks for each hyperfine structure transition are resolved. Additional three peaks appeared on the profile between any pair of major peaks because of the cross-over resonance. The spectral linewidth and the separation ratio in frequency obtained from both optical schematic setups are verified and compared with the calculated values and are in good agreement. Within the scope of the experiment, there is no significant important gained by using the fully counter-propagating DFSAS setup.

The hyperfine structures from the fully counter-propagating setup are not clearly resolved compared to the profiles which were procured from the small cross angle scheme.

5.2 Future Plans

The one of basic and simple technique of optical spectroscopy for exploring the hyperfine structure of atomic vapor was assembled in this research. The hyperfine structure of rubidium provides a frequency reference for stabilizing the ECDL and can be used as a standard frequency for other experiments and applications. For example, it would play an important role in the laser frequency selection for cooling and trapping of rubidium atoms. The DFSAS setup can be compressed into a compact system that saves the work space on an optical table as well as improve simple lab kits for practicing standard techniques in the experimental atomic, molecule, and optical physics.

REFERENCES

[1] W. Demtröder, *Laser Spectroscopy: Volume 1: Basic Principles,* 4th ed., Berlin: Springer-Verlag, 2008.

[2] K. B. MacAdam, A. Steinbach, and C. Wieman, *A narrow band tunable diode laser system with grating feedback, and saturated absorption spectrometer for Cs and Rb,* Am. J. Phys., vol. 60, pp. 1098-1111, Dec. 1992.

[3] R. Paschotta, (2008, December 9), *Encyclopedia of Laser Physics and Technology: Volume A-M,* (1st edition) . [On-line]. Available: www.rp-photonics.com/encyclopedia.html [Mar 12, 2012].

[4] C. Wieman, L. Hollberg, *Using diode laser for atomic physics*, Rev. Sci. Instrum., vol. 62, pp. 1-20, Jan. 1991.

[5] K. Lui, M. G. Littman, *Novel geometry for single mode scanning of tunable lasers*, Opt. Lett., vol. 6, pp. 117-118, Mar. 1981.

[6] C. J. Hawthon, K. P. Weber, R. E. Scholten, *Littrow configuration tunable external cavity diode laser with fixed direction output beam*, Rev. Sci. Instrum, vol. 72, pp. 4477-4479, Dec. 2001.

[7] F. J. Durate, *Tunable Lasers Handbook*, 1st ed., New York: Academic Press, 1995.

[8] C. J. Vale, “Atomic Beam Technique in a Rubidium Vapour Cell.” Ph.D. Thesis, Victoria University of Technology Australia, 2000.

[9] C. J. Foot, *Atomic Physics,* 1st ed., New York: Oxford University Press, 2005.

[10] B. H. Bransden, C. J. Joachain, *Physics of atoms and molecules*, 1st ed., New York: Longman, 1983.

[11] H. E. White, *Introduction to Atomic Spectra,* 1st ed., New York: McGraw-Hill, 1934.

[12] D. W. Preston, *Doppler-free saturated absorption: Laser spectroscopy,* Am. J. Phys., vol. 64, pp. 1432-1436, Nov. 1996.

[13] D. A. Steck, *Rubidium 85 D Line Data*, [On-line], Available: steck.us/alkalidata [Dec. 23, 2010]

[14] D. A. Steck, *Rubidium 87 D Line Data*, [On-line], Available: steck.us/alkalidata [Dec. 23, 2010]

[15] H. E. White, A. Y. Eliason, *Relative Intensity Tables for Spectrum Lines*, Phys. Rev., vol. 44, pp. 753-756, Nov. 1933.

[16] M. Breining, "FM Saturation Spectroscopy." Internet: electron9.phys.utk.edu/optics507/modules/m10/saturation.htm, Apr. 1, 2008 [Mar. 2, 2012]

[17] B. M. Tissue, Spectroscopy Hypermedia on the Internet (1995, May), *Spectroscopy, 10,* 19-21.

[18] Y. Lui, J. Lin, G. Huang, Y. Guo, C. Duan, *Simple empirical analytical approximation to the Voigt profile*, JOSA B, vol. 18, pp. 666-672, May 2001.

[19] D. E. Sporles, "Laser Spectroscopy and Magneto-Optical Trapping of Rubidium Atoms." M.Sc. Thesis, Stony Brook University, 2008.

[20] J. Ye, Advanced Optics Laboratory Manual: "Doppler-free Saturated Absorption Spectroscopy: Laser Spectroscopy" ECE105, Department of Electrical, Computer, and Energy Engineering, University of Colorado at Boulder, 2012.

[21] T. W. Hänsch, I. S. Shahin, A. L. Schawlow, *High-Resolution Saturation Spectroscopy of the Sodium D Lines with a Pulsed Tunable Dye Laser*, Phys. Rev. Lett., vol. 27, pp. 707-710, Sep. 1971.

[22] H. J. Metcalf, P. Straten, *Laser Cooling and Trapping,* 1st ed., New York: Springer, 1999.

[23] G. K. Woodgate, *Elementary atomic structure,* 1st ed., New York: McGraw-Hill, 1970.

[24] E. G. Loewen, M. Nevière, D. Maystre, *Grating efficiency theory as it applies to blazed and holographic gratings*, AO, vol. 16, pp. 2711-2721, Oct. 1977.

[25] E. G. Loewen, E. Popov, *Diffraction Gratings and Applications*, New York : Marcel Dekker, 1997.

[26] N. Thaicharoen, "Light Assisted Collision of Cold Atoms in an Optical Dipole Trap." M.Sc. Thesis, Chiang Mai University, Thailand, 2012.

APPENDICES

Appendix A

GRATING OF THE ECDL

In the Littrow configuration of the ECDL, the grating is a wavelength selective element to send optical feedback of the first order diffracted laser beam into the diode. In this work, the atomic specimen is rubidium. The interested electronic transitions of hyperfine structure were observed corresponds to the optical transitions at wavelength 780 nm. Thus, the wavelength at 780 nm was set in this ECDL work.

In the Littrow configuration [4] the grating angle is fixed as 45 degree, so the groove of the grating that will suit in this work can be calculated by grating equation (2),

$$\lambda = 2d\sin\theta.$$

So that,

$$\begin{aligned} 780\,\mathrm{nm} &= 2d\sin 45^{\circ} \\ d &= \frac{2\sin 45^{\circ}}{780\,\mathrm{nm}} \\ d &\approx 1{,}800\ \mathrm{mm}^{-1} \end{aligned}$$

Thus the groove spacing of the grating in the ECDL is 1,800 lines per mm.

AAppendix B

TUNING THE ECDL

The method of tuning the self-made ECDL was described in much more details than that mentioned in Chapter 3.The process was separated into two parts, the coarse and fine tuning, that was described as follows:

- **Coarse Tuning**
    1. Apply current to the ECDL so that the diode laser lases.
    2. Feed the optical feedback, the first order laser beam which was diffracted from the diffraction grating, back into the diode laser. May use a piece of paper with a small hole for examining the optical feedback from the grating. Both knobs, horizontal and vertical knob, need to be adjusted.

- **Fine Tuning**
    1. After feeding the optical feedback into the diode laser, decrease the applied current and look for the threshold of the diode laser.
    2. Use a power meter to observe an emitted power from the ECDL.
    3. Adjust the horizontal and vertical knob respectively to align the optical feedback finely into the diode laser. If the feedback is sent into the diode, the

laser output power will increase significantly. If not, the output power of the ECDL will maintain at the same value. For the latter case, go back to the coarse tuning to align the optical feedback back into the diode.

4. If the output power of the ECDL increases significantly around the threshold current, at this point the output power is very sensitive to a slight adjustment of the horizontal knob of the ECDL.
5. Find the best threshold current of the ECDL with the process 3 and 4. The best threshold current is the lowest current that the diode laser lase.
6. Increase the applied current to the ECDL to make the laser lase. Next, use the spectrometer to determine the wavelength of the laser emitted from the ECDL.
7. At this step, if the optical feedback is fed well into the diode, the laser wavelength will respond to the horizontal knob adjustment, i.e. the laser wavelength will follow the adjustment of the horizontal knob. This point is called the tunable range of the ECDL.
8. If the wavelength of the ECDL cannot be tuned into the required wavelength, the temperature of the ECDL must be adjusted into the operating temperature of the ECDL that will emit the required wavelength. (the laser wavelength also depends on the applied current and working temperature)
9. Use the Fabry-Perot interferometer to observe frequency modes of the emitted laser. The applied current to the ECDL as well as the horizontal knob requires the adjustment to achieve a single mode laser.
10. After obtaining the tunable wavelength and a single mode, the atomic fluorescence observing from a CCTV monitor is required to obtain the spectroscopy of a rubidium gas in a referenced cell. If the fluorescence does

not appear, this means the wavelength of the laser is not in a working range. Go back to process 3.

11. After finishing process 9, if the wavelength of laser at the single mode operation with fluorescence observed, the emitted laser from the ECDL is ready to be used in the experiment.

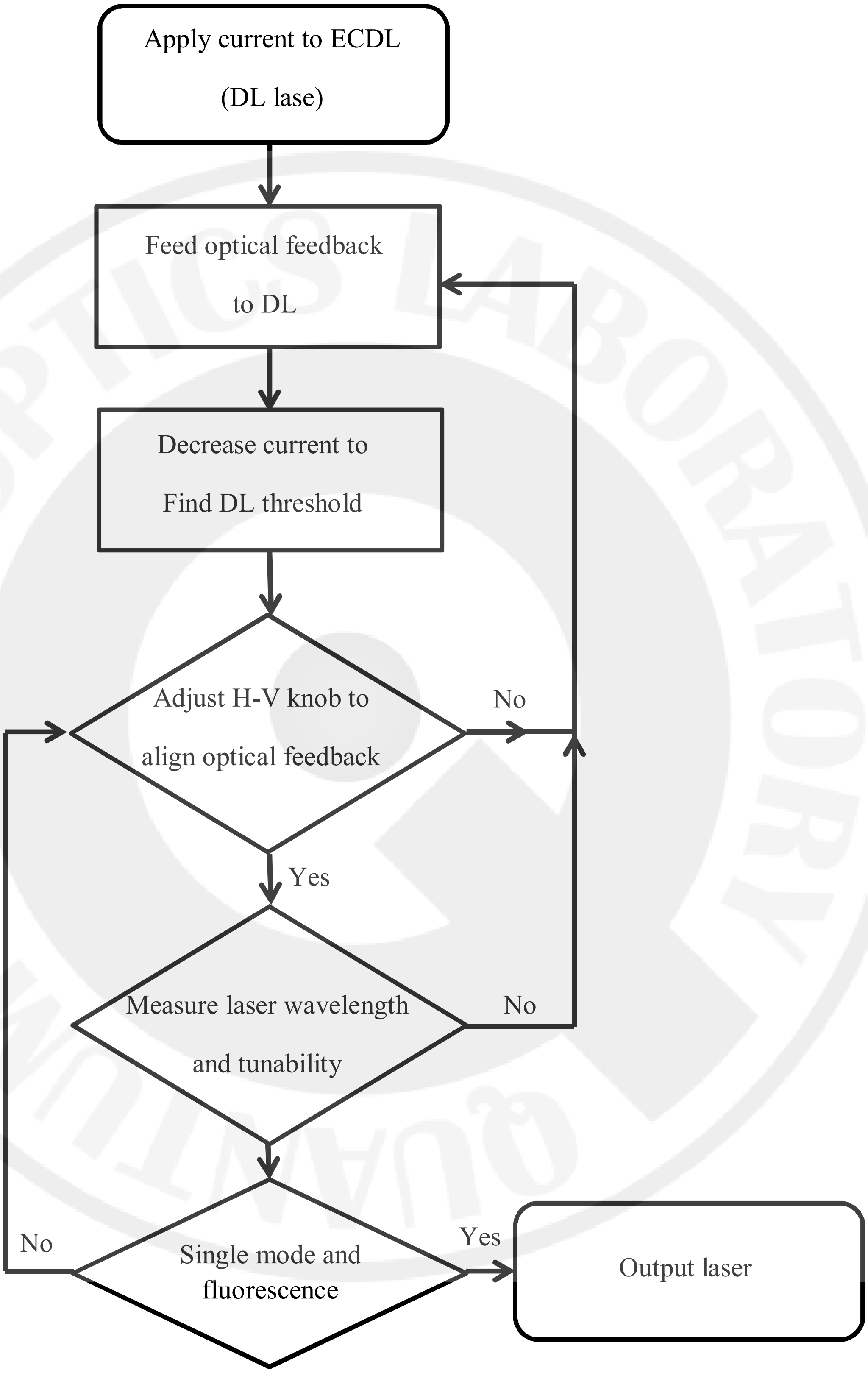

Figure B1 Block diagram of tuning the self-made ECDL method**.** DL is diode laser, H-V knob is horizontal and vertical knob.

Appendix C

PHOTODIODE SPECIFICATION

Silicon PIN Photodiode (Osram, SFH 213)

Feature

- Wavelength range ($S_{10\%}$) 400 nm to 1100 nm
- Short switching time (typ. 5 ns)
- 5 nm LED plastic package

Application

- Industrial electronics
- For control and drive circuits
- High speed photointerrupters

Maximum Ratings

Parameter	Symbol	Value	Unit
Operating and Storage temperature range	T_{op} ; T_{stg}	-40 … +100	ºC
Reverse voltage	V_{R}	20	V
	$V_{\mathrm{R}}(t < 2\ \mathrm{min})$	50	V
Total power dissipation	P_{tot}	150	mW

Characteristics ($T_A = 25^{\circ}C$)

Parameter	Symbol	Value	Unit
Photocurrent $V_R = 5$ V, standard light A, $T = 2856$ K, $E_V = 1000$ lx	I_P	135 (≥ 100)	μA
Wavelength of max. sensitivity	$\lambda_{S\ max}$	850	nm
Spectral range of sensitivity $S = 10\%$ of S_{max}	λ	400 … 1100	nm
Radiant sensitive area	A	1	mm^2
Dimensions of radiant sensitive area	$L \times W$	1 × 1	mm×mm
Half angle	φ	±10	deg.
Dark current	I_R	1 (≤ 5)	nA
Spectral sensitivity, $\lambda = 870$ nm	S_λ	0.62	A/W
Quantum yield, $\lambda = 870$ nm	η	0.89	Photon
Open-circuit voltage $E_V = 1000$ lx, standard light A, $T = 2856$ K	V_o	430 (≥ 350)	mV
Short-circuit current $E_V = 1000$ lx, standard light A, $T = 2856$ K	I_{SC}	125	μA
Rise and fall time of the photocurrent $R_L = 50\ \Omega$; $V_R = 20$ V; $\lambda = 850$ nm	t_r , t_f	5	ns
Forward voltage, $I_F = 80$ mA, $E = 0$	V_F	1.3	V
Capacitance, $V_R = 0$ V, $f = 1$ MHz, $E = 0$	C_0	11	pF
Temperature coefficient of V_0	TC_V	-2.6	mV/K
Temperature coefficient of I_{SC} Standard light A, $\lambda = 870$ nm	TC_I	0.18	%/K
Noise equipment power $V_R = 10$ V, $\lambda = 870$ nm	NEP	2.9×10^{-14}	$\frac{W}{\sqrt{Hz}}$
Detection limit	D^*	$3.5 \times 10^{1}2$	$\frac{cm \times \sqrt{Hz}}{W}$

Relative Spectral Sensitivity SFH 213, $S_{\mathrm{rel}} = f(\lambda)$

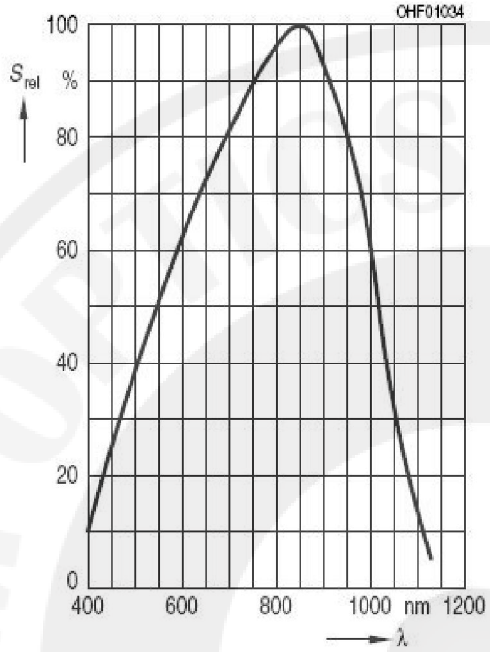

Photocurrent $I_P = f(E_v)$, $V_R = 5$ V Open-Circuit Voltage $V_O = f(E_v)$ SFH 213

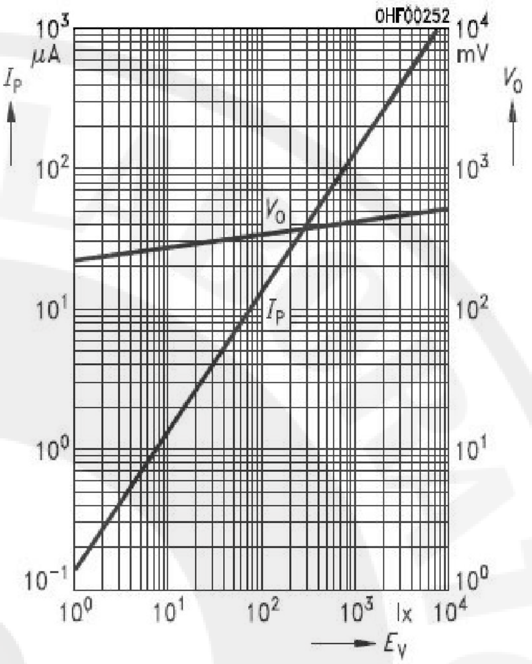

Total Power Dissipation $P_{\mathrm{tot}} = f(T_A)$

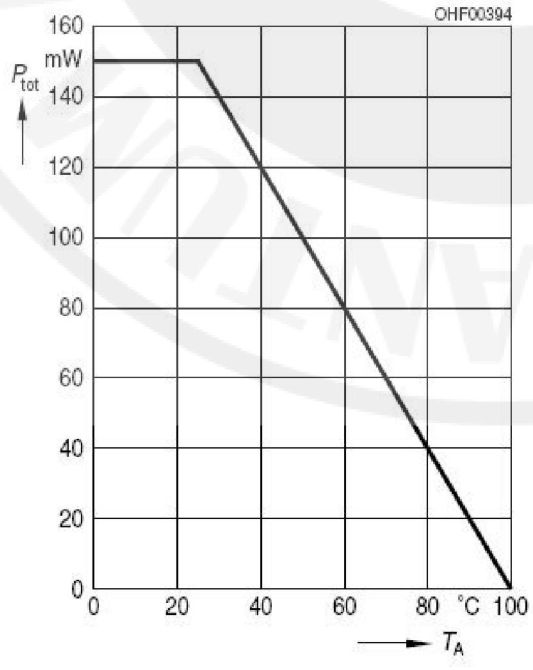

Dark Current $I_R = f(V_R)$, $E = 0$

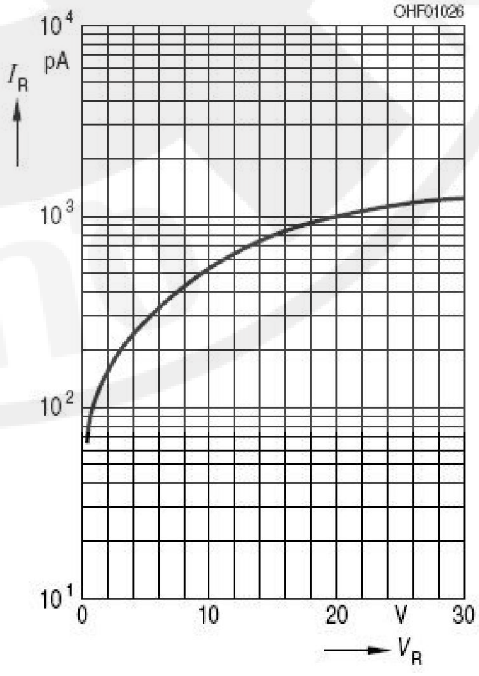

Directional Characteristics

$S_{\mathrm{rel}} = f(\varphi)$

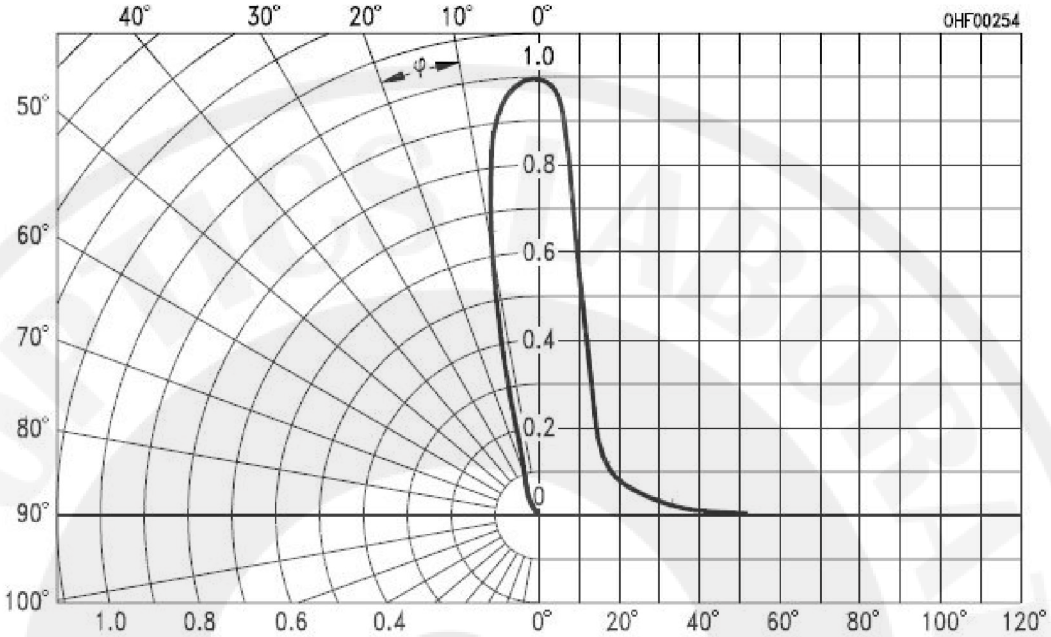

(All figures in Appendix C reproduced from OSRAM data sheet)

Appendix D

CALCULATIONS

D.1 Numbers of Atoms in Rubidium Vapor Cell

The rubidium vapor cell, which was used in the work, was a Pyrex cell of Triad Technology Inc. (TT-RB-75-V-P). The physical dimension of the glass cell was provided in Figure D1.

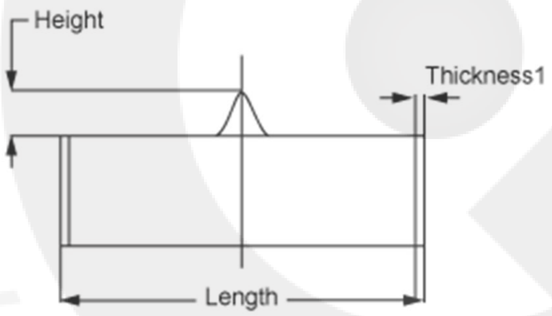

Figure D1 The physical dimensions of the rubidium vapor cell.

Window Material: Pyrex
Stem Height: < 10 mm
Cell Diameter: 25mm
Window Angle: 0°
Window Type: Flat
Window Thickness: 3 mm
Window Surface: 60-40
Quality: Scratch & Dig
Pressure: $> 1 \times 10^{-7}$ Torr
Fill Temperature: 25ºC

The amount of rubidium atoms was simply calculated by using the ideal gas equation,

$$PV = nRT, \tag{D.1}$$

where P is the pressure of the gas, V is the volume of the gas, n is the amount of substance of gas (also known as number of moles), T is the temperature of the gas, and R is the universal gas constant, equal to the product of Boltzmann's constant and Avogadro's constant.

According to the data of the glass cell and equation (D.1), the numbers of rubidium atoms in the vapor cell was determined with the given data from Figure D1:

- The pressure of the gas: $P = (1\times10^{-7}\,\text{Torr})(1.31\times10^{-3}\text{atm/Torr}) = 1.31\times10^{-10}\text{atm}$
- The volume of the gas: $V = \pi r^2 h = \pi(25\ \text{mm})^2(7.18\ \text{mm}) = 1.41\times10^{-5}\ \text{m}^3$
- The temperature of the gas: $T = 298\ \text{K}$

Therefore, the mole of rubidium atoms in the cell was $n = \dfrac{RT}{PV} = 7.455\times10^{-19}$ mole.

By multiplying the Avogadro's number to the number of mole, the amount of atoms was also determined as 4.488×10^5 atoms.

D.2 Average Velocity of Rubidium Atoms in Vapor Cell

Traditionally, the experiment would be conducted at room temperature, the investigation of atoms or molecules in gaseous spectroscopy could be modeled with the thermal-kinetic model of the energy of gas.

$$\frac{1}{2}m\tilde{v}^2 = \frac{3}{2}k_B T, \tag{D.2}$$

where m is the mass of the atom, $\tilde{v}$ is the mean velocity, k_B is the Boltzmann constant, and T is the temperature in Kelvin.

Experimentally, the temperature was $21^{\circ}C$ or 294 K and the atomic specie was rubidium with its mass 85.4678 amu. Thus the average velocity of the rubidium in the vapor cell was examined as

$$\begin{aligned}
\tilde{v} &= \sqrt{\frac{3k_B T}{m}} \\
\tilde{v} &= \sqrt{\frac{3\left(1.38\times10^{23}\ \mathrm{m}^2\cdot\mathrm{kg}\cdot\mathrm{s}^{-2}\cdot\mathrm{K}^{-1}\right)\left(294\ \mathrm{K}\right)}{\left(85.4678\ \mathrm{amu}\right)\left(1.66\times10^{-27}\ \mathrm{kg/amu}\right)}} \\
\tilde{v} &= 292.899\ \mathrm{m/s}
\end{aligned}$$

D.3 The Doppler Broadening Linewidth

In conventional laser spectroscopy, the Doppler broadening arose because of the thermal (Maxwellian) distribution of velocities of the atoms. The lineshape of the Doppler broadening was also the Gaussian lineshape. The Doppler linewidth was calculated from a full width at half maximum of the Gaussian distribution as

$$\delta v_D = \sqrt{8k_B \ln 2}\,\frac{\upsilon_1}{c}\sqrt{\frac{T}{m}}, \tag{D.3}$$

where υ_1 is the resonance frequency in hertz, m is the mass in kilogram, T is the temperature in Kelvin, and c is the speed of light. For rubidium in this case, the Doppler linewidth was determined as

$$\delta v_D = \sqrt{8\left(1.38\times10^{23}\ \mathrm{m}^2\cdot\mathrm{kg}\cdot\mathrm{s}^{-2}\cdot\mathrm{K}^{-1}\right)\ln 2}\,\frac{\left(c/780\mathrm{nm}\right)}{c}\sqrt{\frac{\left(294\ \mathrm{K}\right)}{m}},$$

$\delta v_D = 511.93\ \mathrm{MHz}$ for ^{85}Rb and $\delta v_D = 515.41\ \mathrm{MHz}$ for ^{87}Rb, respectively.

Appendix E

EQUIPMENT LIST FOR THE DFSAS

All of equipment for DFSAS setup was listed as shown in Table D1. In order to construct the self-made ECDL, the details of mechanical drawing and electronic circuits of current and temperature controller unit were described in [26]

Table E1 Details of components for setting up the DFSAS.

Type	Part Number	Company	Details
Laser diode	L785P100	Thorlabs	785 nm, 90 mW CW (220 mW Pulsed), Ø5.6 mm, A Pin Code
Collimation tube	LT110P-B	Thorlabs	Collimation Tube with Optic for Ø5.6 and Ø9 mm Laser Diodes, f = 6.24 mm
Mirror mount	U100-P	Newport	Precision Platform Miror Mount, 2.0 × 2.0 in., No Actuators, 8-32 (M4) CLR
Grating	33001FL02-330H	Newport	15 × 15 × 3.2 mm, 1800 Groove, 500 nm, Holographic Grating
Peltier	TEC1-12710	HB Corporation	40×40×3.3mm,10A/15.8Vmax. Qmax 89W,127 couples
Knob	AJS100-0.5K	Newport	High Precision Large Knob Adjustment Screw, 12.7 mm
Power meter	PM100USB	Throlabs	USB Power and Energy Meter Interface for C-Type Sensors
Spectrometer	CCS175	Thorlabs	Compact Spectrometer 500 - 1000 nm
Fabry-Perot interferometer	SA210-5B	Thorlabs	535-820 nm, Scanning Fabry-Perot Interferometer, 10 GHz FSR
Half-wave plate	WPH10M-780	Thorlabs	Ø1" Zero-Order Half-Wave Plate, SM1-Threaded Mount, 780 nm

Table E2(Continued) Details of components for setting up the DFSAS.

Type	Part Number	Company	Details
Beam splitter	PBS252	Thorlabs	620-1000 nm Polarizing Beamsplitter Cube, 25.4 mm
Rb vapor cell	TT-RB-75-V-P	Triad Technology	Rubidium, Pyrex Cell 25 × 75 mm
Optical isolator	IO-3-780-HP	Thorlabs	Free-Space Isolator, 780 nm, Ø2.7 mm Max Beam, 15 W Max
Miror	BB05-E03	Thorlabs	Ø1/2" Broadband Dielectric Mirror, 750-1100 nm
Photodiode	SFH 213	Osram	PIN Photodiode, 5mm (T1 ¾) Plastic Package, Half angle ±10 °, Radiant Sensitive Area 1 x 1 mm²

CURRICULUM VITAE

Name	Mr. Athip Chayakul
Date of Birth	December 19th, 1986.
Education	
2005-2009	Bachelor of Science (Physics), First Class Honor Department of Physics, Faculty of Science, Prince of Songkla University, Thailand Cumulative GPA 3.83/4.00
2002-2005	Suratpittaya School, Surat Thani, Thailand Cumulative GPA 3.91/4.00
Scholarship	
2005-2012	Development and Promotion of Science and Technology Talent Project (DPST) of the Institute for the Promotion of Teaching Science and Technology (IPST), Ministry of Science and Technology

Experience

2009-2012	Quantum Atom Optics Laboratory, Chiang Mai University, Thailand
2010	National Institute of Metrology (Thailand), Pathum Thani, Thailand
2008	Theoretical Physics Research Unit, Prince of Songkla University, Thailand

Teaching Experience

2012	Teaching Assistant in PHYS207314 Advanced Physics Laboratory II for the 3rd year undergraduate students
2010-2012	Teaching Assistant in PHYS207401 Quantum Mechanics I for the 3rd year undergraduate students Teaching Assistant in PHYS207402 Quantum Mechanics II for the 3rd year undergraduate students
2008	Tutor of PHYS332-306 Introductory Quantum Mechanics for the 3rd year undergraduate students

Presentation

2012 “A Study of Hyperfine Structure of Rubidium-85 for the Magneto-Optical Trap”

AGRC 2012, The 1st ASEAS Plus Three Graduate Research Congress, Chiang Mai, Thailand

2012 “A Study of Hyperfine Structure of Rubidium-85”

Siam Physics Congress 2012 (SPC2012), Phra Nakhon Si Ayutthaya, Thailand

2011 “Doppler-Free Saturated Absorption Spectroscopy System for Studying of the Hyperfine Structure of Rubidium”

The 6th Conference on Science and Technology for Youths, Bangkok, Thailand

Publications

A. Chayakul, T. Poomaradee, P. Sompet, N. Chattrapiban, and W. Anukool, 2012, “A Study of Hyperfine Structure of Rubidium-85 for the Magneto-Optical Trap,” Proceeding of The 1st ASEAN Plus Three Graduate Research Congrees, Chiang Mai, Thailand

N. Thaicharoen, *A. Chayakul*, P. Sompet, N. Chattrapiban, and W. Anukool, 2012, “The First Magneto-Optical Trap in Thailand and Beyond,” Proceeding of The 1st ASEAN Plus Three Graduate Research Congrees, Chiang Mai, Thailand